

# Bosenova collapse of axion cloud around a rotating black hole

Hiroataka YOSHINO<sup>1</sup> and Hideo KODAMA<sup>1,2</sup>

<sup>1</sup>*Theory Center, Institute of Particles and Nuclear Studies, KEK, Tsukuba, Ibaraki, 305-0801, Japan*

<sup>2</sup>*Department of Particle and Nuclear Physics, Graduate University for Advanced Studies, Tsukuba 305-0801, Japan*

Motivated by possible existence of stringy axions with ultralight mass, we study the behavior of an axion field around a rapidly rotating black hole (BH) obeying the sine-Gordon equation by numerical simulations. Due to superradiant instability, the axion field extracts the rotational energy of the BH and the nonlinear self-interaction becomes important as the field grows larger. We present clear numerical evidences that the nonlinear effect leads to a collapse of the axion cloud and a subsequent explosive phenomena, which is analogous to the “bosenova” observed in experiments of Bose-Einstein condensate. The criterion for the onset of the bosenova collapse is given. We also discuss the reason why the bosenova happens by constructing an effective theory of a wavepacket model under the nonrelativistic approximation.

## §1. Introduction

Recently, it was pointed out that string theory may be probed through cosmology or astrophysics by observing phenomena caused by “axions”<sup>1),2)</sup> (see Ref. 3) for a review). The axion usually refers to the QCD axion that was introduced to solve the strong CP problem by Peccei and Quinn,<sup>4),5)</sup> and the QCD axion is expected as one of the candidates of the dark matter. In addition to the QCD axion, in the context of string theory, the stringy axions or axionlike particles have been proposed and discussed.<sup>1),2)</sup> In string theory, many moduli arise when extra dimensions are compactified, and some of them are expected to behave as axionlike scalar fields with ultralight mass. The typical expected number of the axionlike particles is 10–100, and it leads to a generic landscape of stringy axions, the so-called “*axiverse*”.

The ultralight axions cause the possibly observable phenomena in cosmology or astrophysics. Suppose that the decay constant  $f_a$  of the axion is order of the GUT scale,  $f_a \approx 10^{16}$  GeV. In the cosmological context, axions with mass from  $10^{-33}$  eV to  $4 \times 10^{-28}$  eV affect the polarization of cosmic microwave background if the Chern-Simons interaction is present, and those with mass from  $4 \times 10^{-28}$  eV to  $3 \times 10^{-18}$  eV may affect the matter power spectrum. On the other hand, in the astrophysical context, axions are expected to cause interesting phenomena around astrophysical black holes (BHs) if they have mass between  $2 \times 10^{-20}$  eV and  $3 \times 10^{-10}$  eV. We focus on axions around an astrophysical BH in this paper.

Suppose an axion field exists around a rotating BH. Although some of the field would be absorbed by the BH, it is expected that the axion field forms a quasi-bound state which may be called the “axion cloud”. Furthermore, the axion cloud is expected to grow by the superradiant instability. The superradiant instability is caused by the fact that the Killing vector field  $(\partial_t)^a$  of the Kerr spacetime becomes

spacelike in the ergoregion, and therefore, the energy of the field can be negative. A mode with negative energy around the horizon is called a superradiant mode. If a quasibound state whose mode function satisfies the superradiant condition is occupied by the axion field, negative energy falls into the BH and the energy outside the horizon (and therefore, the amplitude of the field) increases in time.

The growth rate of the quasibound state of the axion cloud by the superradiant instability is characterized by the imaginary part  $\gamma$  of the angular frequency  $\omega$ , where  $\omega = \omega_0 + i\gamma$ . The value  $\gamma/\mu$  depends on the ratio of one half of the gravitational radius to the Compton wavelength of axion  $\alpha_g := (GM/c^2)/(\hbar/\mu c)$ , or,  $\alpha_g = M\mu$  in the Planck units  $c = G = \hbar = 1$  (hereafter, the Planck units are used unless otherwise specified). The superradiant instability is effective for  $\alpha_g \sim 1$ , and its typical time scale is  $\tau \sim 10^7 M$  for  $\alpha_g \sim 1$ . For a solar-mass BH  $M = M_\odot$  (resp. a supermassive BH  $M = 10^9 M_\odot$ ), the superradiant instability effectively occurs if an axionlike field with mass  $\mu \sim 10^{-10}$  eV (resp.  $\mu \sim 10^{-19}$  eV) exists, and in that case, the typical time scale for the instability is 50 s (resp. 1600 year). Therefore, the time scale for instability is much shorter than the age of the universe and the superradiant instability should become really relevant to astrophysical phenomena.

The expected phenomena caused by the superradiant instability are discussed and summarized in Refs. 1), 2)\*). As the instability proceeds, the axion cloud extracts rotational energy from a BH and gradually becomes heavy (i.e., the number of axions increases). In Ref. 2), the gravitational wave emission was discussed from the viewpoint of the quantum theory. Since the structure of the axion cloud is analogous to the electron cloud of a hydrogen atom, the graviton emission by the level transition of axions can be discussed in analogy with the photon emission by electron's level transition. Another source of graviton emission is the pair annihilation of two axions. On the other hand, the nonlinear self-interaction of axions is also expected to cause important phenomena. In the case of the QCD axions, due to nonperturbative effects associated with instantons, the potential  $U(\Phi)$  becomes periodic as typically described by the trigonometric function  $U(\Phi) = f_a^2 \mu^2 [1 - \cos(\Phi/f_a)]$ . The similar form of the potential can be expected for string axions because their masses are generated also by the instanton effects. Therefore, although the Klein-Gordon equation (i.e.,  $U(\Phi) = (1/2)\mu^2 \Phi^2$ ) gives a good approximation for small  $\Phi/f_a$ , as the field grows large, the nonlinear effects become important.

One of the nonlinear effects is the mode mixing, which is expected to change the field configuration and affect the growth rate of the superradiant instability. Another interesting possibility is the ‘‘bosenova’’. The bosenova was observed in the experiments of the Bose-Einstein condensates (BEC) of Rb85.<sup>7),8)</sup> The interaction between atoms can be controlled in this system, and the interaction was switched from repulsive one to interactive one in that experiment. As a result, the BEC collapsed, but after that, a burst of atoms was observed. This phenomenon was studied also theoretically<sup>9),10),11)</sup> and it was clarified that the implosion is caused by the nonlinear attractive interaction and the burst is induced mainly by atomic loss through three-body recombinations. Since the atomic loss weakens the attractive

---

\*) This problem was also discussed by a different method in Ref. 6).

interaction, the atoms begin to explode due to zero-point kinetic pressure.

In the case of the BH-axion system, we have to take account of the following two possibilities. The first possibility is that an explosive phenomena that is analogous to the bosenova happens as a result of the nonlinear effect. The second possibility is that the nonlinear effect saturates the growth by superradiant instability, as found in various instabilities of nonlinear systems, leading the system to a quasistationary state without explosive phenomena. We have to clarify which is the case, and if phenomena like the bosenova also occurs in the BH-axion system, the details and the observational consequence have to be studied. In order to clarify the strongly nonlinear phenomena, fully nonlinear simulations have to be performed, and this is the purpose of this paper.

We develop a three-dimensional (3D) code to simulate an axion field with a nonlinear potential in a Kerr spacetime. Here, the axion field is treated as a test field, and the background geometry is fixed to be the Kerr spacetime. In most cases, this approximation holds well. The setup of the problem is explained in more detail in Sec. 4.1. In short, our simulations indicate no evidence for saturation, and the bosenova is likely to happen in the final stage of the superradiant instability.

This paper is organized as follows. In the next section, we review the existing studies on the behavior of a massive scalar field and its superradiant instability focusing attention to the aspects closely related to our study. Section 3 explains the technical part, i.e., the formulation, our code, and code tests. In Sec. 4, we present the numerical results of our simulations. After presenting the results of typical two simulations, we discuss whether the bosenova actually happen by performing supplementary simulations. In Sec. 5, we discuss the reason why the bosenova happens in the BH-axion system by constructing an effective theory of an axion cloud model in the nonrelativistic approximation. Section 6 is devoted to summary and discussion. After summarizing our results, the similarity and difference between the bosenova phenomena in the BEC system and in the BH-axion system is discussed. We also roughly estimate whether gravitational radiation emitted in the bosenova can be detected by planned gravitational wave detectors. In Appendix A, the behaviour of the axion field generated by the nonlinear effect is studied using the Green's function approach, taking attention to the consistency with the results of our simulations.

## §2. Superradiant instability

This section is devoted to the review on massive scalar fields in a Kerr spacetime.

### 2.1. Axion field in a Kerr spacetime

The action for the axion field  $\Phi$  in a spacetime of a metric  $g_{ab}$  is

$$S = \int d^4x \sqrt{-g} \left[ -\frac{1}{2} g^{ab} \nabla_a \Phi \nabla_b \Phi - U(\Phi) \right], \quad (2.1)$$

where  $U(\Phi)$  is the potential, i.e.,  $U(\Phi) = (1/2)\mu^2\Phi^2$  for the Klein-Gordon field and  $U(\Phi) = f_a^2\mu^2[1 - \cos(\Phi/f_a)]$  for the axion field with nonlinear self-interaction (i.e., the sine-Gordon field). Here,  $f_a$  is the decay constant whose value depends on the

model. For convenience, we normalize the amplitude of  $\Phi$  with  $f_a$  as

$$\varphi := \Phi/f_a. \quad (2.2)$$

Then, the field equation is

$$\square\varphi - \hat{U}'(\varphi) = 0. \quad (2.3)$$

with  $\hat{U}(\varphi) = U(\Phi)/f_a^2$ . Here,  $\hat{U}' = \mu^2\varphi$  for the Klein-Gordon field and  $\hat{U}' = \mu^2 \sin\varphi$  for the axion field. Therefore, if the value of  $|\varphi|$  is sufficiently small, the axion field can be well approximated by the Klein-Gordon field. However, the nonlinear effect becomes important as  $|\varphi|$  comes close to unity.

The metric of the Kerr spacetime in the Boyer-Lindquist coordinates is given by

$$ds^2 = - \left( \frac{\Delta - a^2 \sin^2 \theta}{\Sigma} \right) dt^2 - \frac{2a \sin^2 \theta (r^2 + a^2 - \Delta)}{\Sigma} dt d\phi \\ + \left[ \frac{(r^2 + a^2)^2 - \Delta a^2 \sin^2 \theta}{\Sigma} \right] \sin^2 \theta d\phi^2 + \frac{\Sigma}{\Delta} dr^2 + \Sigma d\theta^2, \quad (2.4)$$

with

$$\Sigma = r^2 + a^2 \cos^2 \theta, \quad \Delta = r^2 + a^2 - 2Mr. \quad (2.5)$$

Here,  $M$  is the Arnowitt-Deser-Misner (ADM) mass, and  $a$  is the ADM angular momentum per unit mass,  $a = J/M$ . In order to specify the rotation, the nondimensional parameter  $a/M$  is often used. The solutions of  $\Delta = 0$  give the locations of the inner and outer horizons,  $r_{\pm} = M \pm \sqrt{M^2 - a^2}$ , and the event horizon is located at  $r = r_+$ . In the Kerr geometry, the equation for the axion field is

$$-F\varphi_{,tt} - 2a(r^2 + a^2 - \Delta)\varphi_{,t\phi} + \frac{\Delta - a^2 \sin^2 \theta}{\sin^2 \theta} \varphi_{,\phi\phi} + \Delta(\varphi_{,\theta\theta} + \cot \theta \varphi_{,\theta}) \\ + 2r\Delta\varphi_{,r_*} + (r^2 + a^2)^2 \varphi_{,r_* r_*} - \Sigma \Delta \hat{U}'(\varphi) = 0, \quad (2.6)$$

where

$$F := (r^2 + a^2)^2 - \Delta a^2 \sin^2 \theta. \quad (2.7)$$

Here, we introduced the tortoise coordinate by  $dr_* = [(r^2 + a^2)/\Delta]dr$ , or equivalently,

$$r_* = r + \frac{2M}{r_+ - r_-} (r_+ \log |r - r_+| - r_- \log |r - r_-|). \quad (2.8)$$

In the tortoise coordinate  $r_*$ , the horizon is located at  $r_* = -\infty$ .

The scalar field in a Kerr spacetime has conserved quantities. If a Killing vector  $\xi^a$  is present in a spacetime, we can define the conserved current  $P_a = -T_{ab}\xi^b$  that satisfies  $\nabla_a P^a = 0$ . Here,  $T_{ab}$  is the energy-momentum tensor (in the unit  $f_a = 1$ )

$$T_{ab} = \nabla_a \varphi \nabla_b \varphi - \frac{1}{2} g_{ab} \left( \nabla_c \varphi \nabla^c \varphi + 2\hat{U}(\varphi) \right). \quad (2.9)$$

Using this current  $P_a$ , the conserved quantity  $C(t) \equiv C(0)$  can be introduced as

$$C(t) := \bar{C}(t) + \Delta C(t), \quad (2.10)$$

with the quantity  $\bar{C}(t)$  in the region  $r_*^{(\text{in})} \leq r_* \leq r_*^{(\text{out})}$ ,

$$\bar{C}(t) = \int_{\Sigma_t} P_a n^a d\Sigma, \quad (2.11)$$

and the integrated flux toward the horizon at  $r_* = r_*^{(\text{in})}$ ,

$$\Delta C(t) = \int_{r_* = r_*^{(\text{in})}} P_a s^a d\sigma. \quad (2.12)$$

Here, we have assumed the absence of outgoing flux at the outer boundary  $r_* = r_*^{(\text{out})}$ . The integration of the first term  $\bar{C}(t)$  is performed on  $t = \text{const.}$  slice  $\Sigma_t$  in the range  $r_*^{(\text{in})} \leq r_* \leq r_*^{(\text{out})}$  with the past-directed timelike unit normal  $n^a$  and the volume element  $d\Sigma$ , and it represents the conserved quantity contained in the region  $r_*^{(\text{in})} \leq r_* \leq r_*^{(\text{out})}$ . The second term  $\Delta C(t)$  is the integrated flux, where the integration is performed on the hypersurface  $r_* = r_*^{(\text{in})}$  from time zero to  $t$  with the spacelike unit normal  $s^a$  directing toward the horizon and the surface element  $d\sigma$ . The value of  $\Delta C(t)$  indicates the total quantity that has fallen into the BH from time zero to  $t$ . Since the Kerr spacetime possesses two Killing vectors,  $\xi^a = (\partial_t)^a$  and  $(\partial_\phi)^a$ , there exist two conserved quantities: the energy  $E$  and the angular momentum  $J$ .

## 2.2. Superradiant instability

Here, we briefly review the superradiant instability of a massive Klein-Gordon field around a Kerr BH. If the nonlinear terms are absent, the separation of variables is available as follows. Setting  $\varphi = 2\text{Re}[e^{-i\omega t} R(r) S_{\ell m}(\theta) e^{im\phi}]$ , the equations for  $S_{\ell m}(\theta)$  and  $R(r)$  become

$$\frac{1}{\sin\theta} \frac{d}{d\theta} \left( \sin\theta \frac{dS_{\ell m}}{d\theta} \right) + \left[ -k^2 a^2 \cos^2\theta - \frac{m^2}{\sin^2\theta} + E_{\ell m} \right] S_{\ell m} = 0, \quad (2.13)$$

$$\frac{d}{dr} \left( \Delta \frac{dR}{dr} \right) + \left[ \frac{K^2}{\Delta} - \lambda_{\ell m} - \mu^2 r^2 \right] R = 0, \quad (2.14)$$

where

$$K = (r^2 + a^2)\omega - am, \quad (2.15)$$

$$k^2 = \mu^2 - \omega^2, \quad (2.16)$$

and

$$\lambda_{\ell m} = E_{\ell m} + a^2 \omega^2 - 2am\omega. \quad (2.17)$$

Here,  $S_{\ell m}(\theta) e^{im\phi}$  is the spheroidal harmonics, which coincides with the spherical harmonics in the case  $k = 0$ . The angular quantum numbers,  $\ell$  and  $m$ , are integers  $\ell = 0, 1, 2, \dots$  and  $-\ell \leq m \leq \ell$ . The eigenvalue  $E_{\ell m}$  is  $E_{\ell m} = \ell(\ell + 1)$  in the case of  $k = 0$ , while in the case  $k \neq 0$ , it has to be evaluated numerically by the methods of Refs. 12), 13) or by the approximate formulas.<sup>14), 15), 16)</sup>

From the equation (2.14) for the radial function  $R(r)$ , the behavior of  $R(r)$  at  $r_*/M \gg 1$  is described as  $R \sim r^{-1} \exp(\pm kr)$ . If  $\text{Re}[\omega] < \mu$ , the field is bounded

by gravitational interaction and does not escape to infinity. On the other hand, the behavior of  $R(r)$  in the neighborhood of the horizon  $r_*/M \ll -1$  is  $R \sim e^{\pm i\tilde{\omega}r_*}$ , where the plus and minus signs correspond to the outgoing and ingoing modes, respectively. Here,  $\tilde{\omega}$  is defined as  $\tilde{\omega} = \omega - m\Omega_H$  with the angular velocity of the horizon  $\Omega_H = a/(2Mr_+)$ .

Here, let us focus attention to the energy  $E$  of the Klein-Gordon field introduced in Sec. 2.1. Evaluating the energy density with respect to the tortoise coordinate  $r_*$  for the  $t = \text{const.}$  surface, we have  $d\bar{E}/dr_* \simeq 2\omega\tilde{\omega}(r_+^2 + a^2)$  in the neighborhood of the horizon. Here, we have used the ingoing solution  $R \sim e^{-i\tilde{\omega}r_*}$  for  $r_*/M \ll -1$ . On the other hand, the energy flux  $F_E := d(\Delta E)/dt$  toward the horizon can be evaluated as  $F_E \simeq 2\omega\tilde{\omega}(r_+^2 + a^2)$ . Therefore, if waves satisfy the superradiant condition  $0 < \omega < m\Omega_H$  (i.e.,  $\tilde{\omega} < 0$ ), the negative energy distributes in the neighborhood of the horizon and it falls into the BH “at the speed of light” in the coordinates  $(t, r_*)$ .

The negative energy of waves satisfying the superradiant condition leads to an interesting phenomena. Suppose waves satisfying the superradiant condition are incident to a rotating BH. A fraction of waves falls into the BH, and the rest is reflected back to infinity by the centrifugal potential barrier of the BH. Since the negative energy falls into the BH, the reflected waves have greater energy than the initial ingoing waves because of the energy conservation. In other words, reflected waves get amplified. This is called superradiance. The superradiance was proposed and analyzed for the massless Klein-Gordon field first by Zel’dovich.<sup>17), 18)</sup>

Using superradiance, Press and Teukolsky<sup>19)</sup> proposed a mechanism to cause an instability of fields around a rotating BH, which is called the BH bomb. In this mechanism, a mirror is put around a BH. Waves satisfying the superradiant condition are reflected back and forth between the BH horizon and the mirror, and thus, continue to get amplified. As a result, the amplitude of waves exponentially grows in time. The mirror in the BH-bomb model seems to be artificial. However, it was pointed out by Damour *et al.*<sup>20)</sup> that if the field has non-vanishing mass, the reflected waves can fall back to the BH because of the gravitational force on the rest mass. In other words, if the field is in a quasibound state,  $\text{Re}[\omega] < \mu$ , the superradiant instability occurs without putting a mirror. The instability of a massive Klein-Gordon field around a Kerr BH was analytically studied by Detweiler<sup>21)</sup> and Zouros and Eardley.<sup>22)</sup>

Detweiler<sup>21)</sup> analyzed the situation  $\alpha_g := M\mu \simeq M\omega \ll 1$ . In this setup, the solution of the radial function  $R(r)$  can be obtained by the matching method. After the solutions for the distant region and the near-horizon region are obtained separately, they are matched to each other in an overlapping region. After the matching, the solution for a distant region is same as the wavefunction of the eigenstate of a hydrogen atom in quantum mechanics, since the equation for the scalar field is same as the Schrödinger equation for a hydrogen atom with the potential  $e^2/r$  being replaced by  $\alpha_g/r$ . The result of the growth rate for the  $(\ell, m) = (1, 1)$  mode is  $\gamma M = (1/24)\alpha_g^9(a/M)$ .

Zouros and Eardley<sup>22)</sup> assumed  $\alpha_g \gg 1$  and analyzed with the WKB approximation. Introducing a function  $u = \sqrt{r^2 + a^2}R$ , the radial mode equation is rewritten

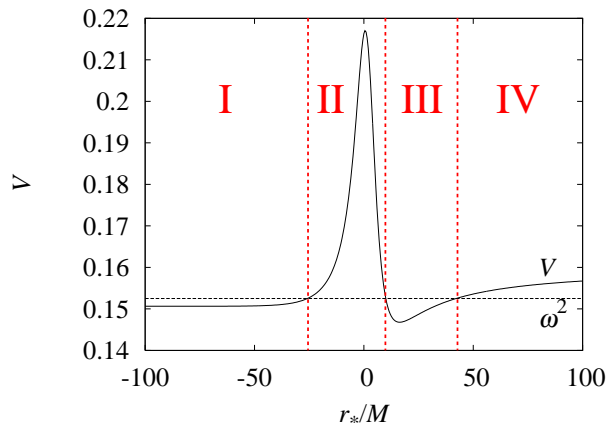


Fig. 1. The potential  $V(\omega, r_*)$  (in the unit  $M = 1$ ) in Eq. (2·18) for a quasibound state of the Klein-Gordon field for situation  $a/M = 0.99$  and  $\alpha_g := M\mu = 0.4$  (solid line). The horizontal dotted line indicates the value of  $\omega^2$ . Here, the imaginary part is ignored. There are four domains I, II, III, and IV, depending on the relation between  $V$  and  $\omega^2$ , and the quasibound state is formed in region III. Due to the tunneling effect, the waves gradually fall into the region I. Because the energy of waves takes a negative value in region I under the superradiant condition, the field in region III is amplified.

as the Schrödinger-type equation:

$$\frac{d^2 u}{dr_*^2} + [\omega^2 - V(\omega, r_*)] u = 0. \quad (2\cdot18)$$

The potential for  $a/M = 0.99$  and  $\alpha_g = 0.4$  is shown in Fig. 1. The potential  $V$  asymptotes to  $\mu^2$  from below for  $r_* \rightarrow \infty$ , and this potential rise plays the role of the mirror. The quasibound state is formed in the region III, and because of the tunneling effect, the mode function gradually escape into the region I as ingoing waves. If these ingoing waves toward the horizon satisfies the superradiant condition, the energy of the quasibound state increases and the wavefunction get amplified in the region III. Their result shows that the growth rate  $M\gamma$  exponentially decreases as  $\alpha_g$  is increased.

In the region where the largest growth rate of instability is expected,  $\alpha_g \sim 1$ , numerical calculations are required. These studies were done in Refs. 23), 24), 25), 26). The most detailed results have been reported by Dolan<sup>26)</sup> by applying Leaver's continued fraction method<sup>12)</sup> to this problem. The continued fraction method was originally developed to calculate the value of quasinormal frequencies numerically, and it enables us to obtain highly accurate values of  $\omega$  for the quasibound state as well. The result is shown in Figs. 6 and 7 of Ref. 26). The largest growth rate is realized for  $(\ell, m) = (1, 1)$ ,  $a/M \simeq 1$ , and  $\alpha_g \simeq 0.4$ , and its value is  $\gamma/\mu \simeq 3 \times 10^{-7}$ . In Ref. 3), we also developed a code to calculate  $\omega$  of the quasibound state and reproduced Dolan's result. As an example, the configuration of the field  $\varphi$  of the  $(\ell, m) = (1, 1)$  mode in the equatorial plane and in the  $(\rho, z)$ -plane (where  $\rho := r \sin \theta$  and  $z := r \cos \theta$ ) are shown as contour plots in the left and right panels of Fig. 2,

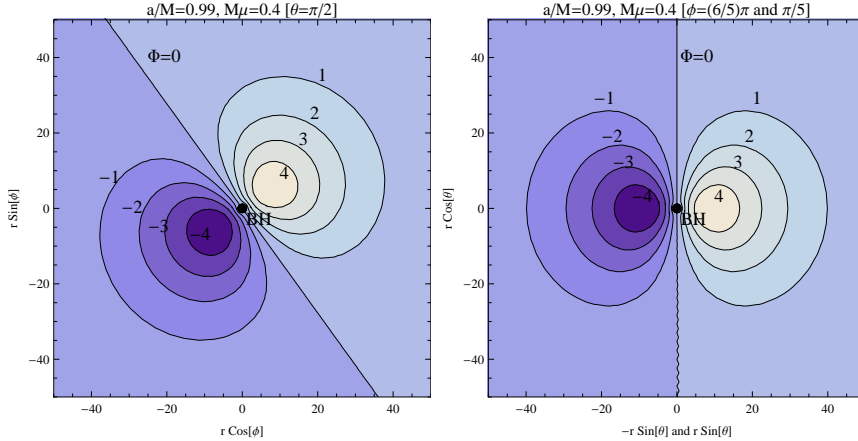


Fig. 2. A snapshot for the contours of the Klein-Gordon field  $\varphi$  of the  $(\ell, m) = (1, 1)$  mode of the quasibound state in the case of  $a/M = 0.99$  and  $\alpha_g := M\mu = 0.4$  in the equatorial plane  $\theta = \pi/2$  (left panel) and in the  $(\rho, z)$ -plane (right panel). Here,  $\rho := r \sin \theta$  and  $z := r \cos \theta$ , and the  $(\rho, z)$ -plane is drawn for the azimuthal angle  $\phi = \pi/5$  and  $(6/5)\pi$  so that the plane crosses the peak of the field.

respectively, for  $a/M = 0.99$  and  $\alpha_g = 0.4$ .

### §3. Numerical method and code

In this section, we explain the technical part of our study. The formulation for solving the axion field around a Kerr BH is explained in Sec. 3.1, and the numerical techniques and code tests are summarized in Sec. 3.2.

#### 3.1. Numerical method

The most important point in simulations of fields in the Kerr background spacetime is to realize the sufficient stability. We found that if a simulation is performed in the Boyer-Lindquist coordinates with central difference method, a numerical instability immediately develops to crash the simulation. This is because the lines with constant spatial coordinates are spacelike in the ergoregion in the Boyer-Lindquist coordinates, and therefore, the frame is propagating superluminally. Although this problem may be avoided by adopting the upwind difference method, we have chosen another method with which greater stability is expected. This method is explained in Secs. 3.1.1 and 3.1.2. We also explain the boundary condition and how to regularize the equation at the poles in Secs. 3.1.3 and 3.1.4, respectively.

##### 3.1.1. ZAMO coordinates

In our method, we realize the numerical stability by adopting the coordinates associated with the zero-angular-momentum observers (ZAMOs). The ZAMOs are observers such that they stay at fixed  $r$  and  $\theta$ , but move in the  $\phi$  direction so that their angular momenta are kept to be zero. Their four-velocity is given by  $u^a = \nabla^a t / \sqrt{-\nabla^b t \nabla_b t}$ , which is timelike everywhere, and they rotate with the angular



velocity

$$\Omega(r, \theta) = \frac{2Mar}{F}, \quad (3.1)$$

where  $F$  is defined in Eq. (2.7). Using this angular velocity, we introduce the new coordinates  $(\tilde{t}, \tilde{\phi}, \tilde{r}, \tilde{\theta})$  as

$$\tilde{t} = t, \quad \tilde{\phi} = \phi - \Omega(r, \theta)t, \quad \tilde{r} = r, \quad \tilde{\theta} = \theta. \quad (3.2)$$

The basis vector of the new time coordinate  $\tilde{t}$  is parallel to  $u^a$ , and therefore, it is timelike everywhere. We call these coordinates the ZAMO coordinates. The equation for the axion field reads

$$\begin{aligned} -F\varphi_{,\tilde{t}\tilde{t}} + \left[ \frac{\Sigma^2 \Delta}{F \sin^2 \tilde{\theta}} + \tilde{t}^2 \Delta \left( \Delta \Omega_{,\tilde{r}}^2 + \Omega_{,\tilde{\theta}}^2 \right) \right] \varphi_{,\tilde{\phi}\tilde{\phi}} + (\tilde{r}^2 + a^2)^2 \varphi_{,\tilde{r}\tilde{r}} + 2\tilde{r} \Delta \varphi_{,\tilde{r}\tilde{\theta}} \\ + \Delta \left( \varphi_{,\tilde{\theta}\tilde{\theta}} + \cot \tilde{\theta} \varphi_{,\tilde{\theta}} \right) - 2\tilde{t} \Delta \left[ (\tilde{r}^2 + a^2) \Omega_{,\tilde{r}} \varphi_{,\tilde{r}\tilde{\phi}} + \Omega_{,\tilde{\theta}} \varphi_{,\tilde{\theta}\tilde{\phi}} \right] \\ - \tilde{t} \Delta \left[ (\Delta \Omega_{,\tilde{r}})_{,\tilde{r}} + (\Omega_{,\tilde{\theta}\tilde{\theta}} + \cot \tilde{\theta} \Omega_{,\tilde{\theta}}) \right] \varphi_{,\tilde{\phi}} - \Sigma \Delta \hat{U}'(\varphi) = 0, \end{aligned} \quad (3.3)$$

in the ZAMO coordinates.

### 3.1.2. Pullback of coordinates

Because the angular velocity  $\Omega$  of a ZAMO becomes larger as it is closer to the horizon, the ZAMO coordinates become distorted in time evolution. This is the shortcoming of the ZAMO coordinates because if the coordinates are distorted, the numerical error grows large, and also, the physical interpretation of the numerical results becomes difficult. We solve this problem by ‘‘pulling back’’ the ZAMO coordinates. Namely, when the ZAMO coordinates become distorted to some extent, we introduce new ZAMO coordinates which are not distorted at that time (i.e., the new ZAMO coordinates agree instantaneously with the Boyer-Lindquist coordinates), and continue time evolution with the new coordinates. Iterating these processes, longterm evolution becomes feasible. Specifically, for  $nT_P \leq t \leq (n+1)T_P$ , we adopt the  $n$ -th ZAMO coordinates  $(\tilde{t}^{(n)}, \tilde{\phi}^{(n)}, \tilde{r}^{(n)}, \tilde{\theta}^{(n)})$  by

$$\tilde{t}^{(n)} = t, \quad \tilde{\phi}^{(n)} = \phi - \Omega(r, \theta)(t - nT_P), \quad \tilde{r}^{(n)} = r, \quad \tilde{\theta}^{(n)} = \theta. \quad (3.4)$$

The numerical data of  $\Phi$  and  $\partial\Phi/\partial\tilde{t}$  in the new coordinates are generated by interpolation. In our numerical calculations, we adopt  $T_P = M/4$ . If we list up the data of  $\Phi$  at time  $t = nT_P$  with  $n = 0, 1, 2, \dots$ , they can be regarded as the data in the Boyer-Lindquist coordinates.

### 3.1.3. Boundary conditions

Since a simulation has to be performed in a finite coordinate region, the coordinate range of  $r_*$  is taken as  $r_*^{(\text{in})} \leq r_* \leq r_*^{(\text{out})}$ . Here, we discuss how to impose the inner and outer boundary conditions at  $r_* = r_*^{(\text{in})}$  and  $r_*^{(\text{out})}$ , respectively.

For a sufficiently small  $r_*^{(\text{in})}$ , we have  $\Delta \simeq 0$  at  $r = r_*^{(\text{in})}$ . Then, the equation for  $\varphi$  in the ZAMO coordinates, Eq. (3.3), becomes

$$-\varphi_{,\tilde{t}\tilde{t}} + \varphi_{,\tilde{r}\tilde{r}} \simeq 0. \quad (3.5)$$

Therefore, the in- and out- going modes are clearly separated, and we can impose the purely ingoing boundary condition in the standard manner. Typically, we adopt  $r_*^{(\text{in})}/M = -200$ .

At  $r = r_*^{(\text{out})}$ , we adopt the fixed boundary condition,  $\varphi = 0$ . When the axion field is in a bound state, this boundary condition gives a good approximation. If outgoing waves are generated, the outer boundary becomes reflective, which is quite artificial. In such a case, we avoid the problem by adopting sufficiently large  $r_*^{(\text{out})}$ . Typically, the outer boundary is located between  $r_*^{(\text{out})}/M = 200$  and 1000 depending on the situation.

#### 3.1.4. Regularization at poles

Since the two poles  $\tilde{\theta} = 0$  and  $\pi$  are coordinate singularities, regularization of the equation is required at the poles. For this purpose, we introduce new coordinates  $(x, y)$  by

$$x = \tilde{\theta} \cos \tilde{\phi}, \quad y = \tilde{\theta} \sin \tilde{\phi}, \quad (3.6)$$

in the neighborhood of each pole. Rewriting Eq. (3.3) with these coordinates and taking the limit  $\tilde{\theta} \rightarrow 0$  or  $\pi$ , we obtain

$$-F\varphi_{,\tilde{t}\tilde{t}} + (\tilde{r}^2 + a^2)^2\varphi_{,\tilde{r}_*\tilde{r}_*} + \Delta \left[ \varphi_{,xx} + \varphi_{,yy} + 2\tilde{r}\Delta\varphi_{,\tilde{r}_*} - \Sigma\hat{U}'(\varphi) \right] = 0. \quad (3.7)$$

Here,  $\varphi_{,xx}$  can be evaluated by the data at the grids on  $\tilde{\phi} = 0$  and  $\pi$ , and  $\varphi_{,yy}$  by the data at the grids on  $\tilde{\phi} = \pi/2$  and  $(3/2)\pi$ . Therefore, the data of grids at the poles can be evolved toward the next time step with this equation.

### 3.2. Code and code checks

Our code is a three-dimensional (3D) code of the ZAMO coordinates  $(\tilde{r}_*, \tilde{\theta}, \tilde{\phi})$ . The sixth-order finite differencing method is used in spatial directions, and time evolution is proceeded with the fourth-order Runge-Kutta method. Typically, we used the grid size  $\Delta r_*/M = 0.5$  and  $\Delta\theta = \Delta\phi = \pi/30$ . When the spherical-polar coordinates are used, the Courant condition for the time step becomes severe and it has to be chosen so that  $\Delta t \lesssim \min[(F/\Sigma\Delta^{1/2})_{\theta=0}\Delta\theta\Delta\phi]$  from Eq. (3.3). Here we adopt the value of the time step as  $\Delta t = (3/2\pi)\Delta\theta\Delta r_*$  in order to realize the sufficient stability of our simulations. In doing the ‘‘pullback’’ of the ZAMO coordinates addressed in Sec. 3.1.2, the interpolation of data is necessary, and we applied the seventh-order Lagrange interpolation.

In order to validate the code, we have to perform test simulations. The code checks have been done in the three following manners, as explained one by one below.

#### 3.2.1. Comparison with semianalytic solution

The first check is to simulate time evolution of the quasibound state of the linear Klein-Gordon equation and compare the numerical data with the semianalytic solution. Here, we choose the BH with the rotation parameter  $a/M = 0.99$  and the Klein-Gordon field of mass  $\mu = 0.4/M$ . The semianalytic solution  $\varphi = e^{-i\omega t} R(r)S(\theta)e^{im\phi}$  can be obtained by using the approximate formula for  $S_{\ell m}(\theta)$ <sup>15)</sup> and numerically calculating  $\omega$  and  $R(r)$  using the continued fraction method.<sup>12), 26)</sup> The time evolution

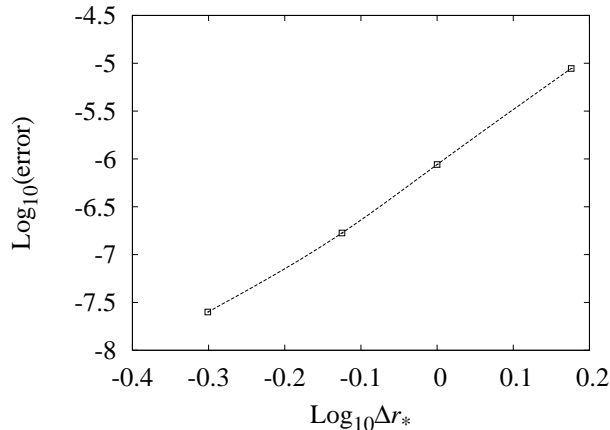


Fig. 3. The relation between the grid size  $\Delta r_*$  (with unit  $M = 1$ ) and the numerical error evaluated at  $t = 12.5M$ . The error decreases as  $\Delta r_*$  is increased, and the slope of the curve is  $\simeq 5$ . This reflects our combined fourth- and sixth-order scheme.

was performed up to  $t = 100M$ , and the numerical data were confirmed to agree well with the semianalytic solution.

The imaginary part  $\gamma$  of frequency  $\omega = \omega_0 + i\gamma$  of the semianalytic solution gives the correct growth rate of the superradiant instability. In the present setup, it is calculated as  $\gamma/\mu \simeq 3.311 \times 10^{-7}$  by the continued fraction method. In order to check to what extent the superradiant instability is correctly realized in our numerical simulation, we calculated the energy  $\bar{E}(t)$  in the region  $r_*^{(\text{in})} \leq r_* \leq r_*^{(\text{out})}$  [see Eq. (2.11) in Sec. 2.1 for the definition of  $\bar{E}(t)$ ], and evaluated  $\gamma = (d\bar{E}/dt)/2\bar{E} \simeq [\bar{E}(t_f) - \bar{E}(0)]/[2t_f\bar{E}(0)]$  with  $t_f = 100M$ . The numerical result performed in the grid sizes mentioned above is  $\gamma/\mu \simeq 3.255 \times 10^{-7}$ : The deviation from the value of the semianalytic solution is about 1.7%. Therefore, our code has the ability to describe the energy extraction by the superradiant instability fairly accurately.

### 3.2.2. Convergence with respect to grid size

One of the standard tests of numerical simulations is to check whether the numerical solution converges as the grid size is made smaller. For this purpose, we adopt the numerical solution of  $\Delta r_*/M = 1/6$  as the reference solution, and evaluated the deviation of the numerical solutions with several grid sizes. Here, we adopted  $\varphi(0) = \exp[(r_*/30)^2] \sin \theta \cos \phi$  and  $\dot{\varphi}(0) = 0$  as the initial condition and evolved the data until  $t/M = 12.5$  for the parameters  $\alpha_g := M\mu = 0.4$  and  $a/M = 0.99$ . Figure 3 shows the relation between  $\log_{10} \Delta r_*$  and  $\log_{10}(\text{error})$ . Since we use the sixth- and fourth-order schemes in the space and time directions, the curve is expected to have slope between four and six. Actually, the slope is  $\sim 5$  in this figure. This result reflects the adopted scheme, and supports the validity of our code.

### 3.2.3. Conserved quantities

As discussed in Sec. 2.2, we have the two conserved quantities, the energy  $E$  and the angular momentum  $J$ . In actual simulations, these quantities slightly change in

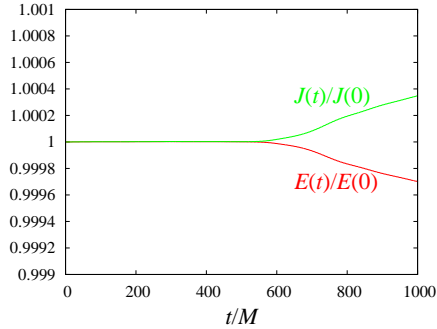


Fig. 4. The values of total energy and angular momentum normalized by the initial values,  $E(t)/E(0)$  and  $J(t)/J(0)$ , as functions of time (the solid line and the dashed line, respectively). Deviation from unity indicates the amount of numerical error. The error is less than 0.04% at  $t/M = 1000$ .

time because of numerical error. Therefore, the deviations of the values  $E(t)/E(0)$  and  $J(t)/J(0)$  from unity give indicators for the accumulated numerical errors.

Figure 4 shows the values of  $E(t)/E(0)$  and  $J(t)/J(0)$  as functions of time  $t/M$ . Here, we show the results for the simulation of axion mass  $\alpha_g = 0.4$  around a BH with  $a/M = 0.99$  for initial amplitude  $\varphi_{\text{peak}}(0) = 0.7$  [i.e., simulation (B) of Sec. 4.2.2]. The deviation from unity is negligible for  $t/M \lesssim 500$ . For  $t \gtrsim 500$ , the deviations linearly increase. This is because the “bosonova” happens and some part of the axion field distributes at a distant place. As a result, small error in the field value results in large errors of  $E(t)$  and  $J(t)$  because large volume element is multiplied there. Nevertheless the deviations from unity are less than 0.04% at  $t/M = 1000$  for both  $E(t)/E(0)$  and  $J(t)/J(0)$ .

As found above, we checked the validity of our code in three ways, and therefore, we can trust the results of our longterm simulations.

#### §4. Numerical results

Now we present the numerical results. In Sec. 4.1, we describe the setup of the system and the initial conditions. In Sec. 4.2, we show the results of typical two simulations [referred as simulations (A) and (B)], for which the effect of nonlinearity is weak and strong, respectively. This helps us to understand how nonlinearity works in this system. Then, in Sec. 4.3, we discuss what actually happens in the final stage of the superradiant instability, taking special attention to whether the bosonova happens or not.

##### 4.1. Setup

In order to study the nonlinear self-interaction of an axion field, we numerically solve the sine-Gordon equation  $\square\varphi - \mu^2 \sin\varphi = 0$  in a Kerr spacetime. For simplicity, we consider an axion cloud with mass  $\alpha_g := M\mu = 0.4$  around a Kerr BH with the rotational parameter  $a/M = 0.99$ . As the initial condition, we adopt the quasibound state solution to the linear Klein-Gordon field corresponding to the

Table I. Performed two simulations, (A) and (B), in Sec. 4.2. “KG bound state” means that the initial condition is adopted as the quasibound state of Klein-Gordon field of  $(\ell, m) = (1, 1)$  mode, and  $\varphi_{\text{peak}}(0)$  indicates the initial amplitude.

Simulations	Initial condition	$E/[(f_a/M_p)^2 M]$	nonlinearity
(A)	KG bound state, $\varphi_{\text{peak}}^{(A)}(0) = 0.60$	1430	weak
(B)	KG bound state, $\varphi_{\text{peak}}^{(B)}(0) = 0.70$	1862	strong

$(\ell, m) = (1, 1)$  mode. Namely, the configuration shown in Fig. 2 are used (but changing the amplitude of the oscillation). If nonlinear terms are absent (i.e., in the case of the Klein-Gordon field), the frequency is  $\omega = \omega_0 + i\gamma$ , where the real part is  $\omega_0 M \simeq 0.39$  and the imaginary part (i.e., the growth rate by the superradiant instability) is  $\gamma M \simeq 1.32 \times 10^{-7}$ , which is the approximately largest possible growth rate. These are natural setups, because we consider the situation where the axion fields have grown due to the superradiant instability and, at least for small  $|\varphi|$ , such situations should be well approximated by the quasibound state of the Klein-Gordon field. As typical examples, we present the results of two simulations with different initial amplitude [simulations (A) and (B) in Secs. 4.2.1 and 4.2.2, respectively, see Table I]. In Sec. 4.3, we discuss what actually happens as a result of superradiant instability by performing supplementary simulations starting with initial conditions that is expected to be more natural compared to those of the simulations (A) and (B).

#### 4.2. Typical two simulations

Now, we present the results of the simulations (A) and (B).

##### 4.2.1. Simulation (A): A weakly nonlinear case

In the simulation (A), we choose the initial amplitude to be  $\varphi_{\text{peak}}(0) = 0.6$ . The effect of the nonlinearity can be evaluated by  $\Delta_{\text{NL}} := (\varphi - \sin \varphi)/\varphi \simeq \varphi^2/6$ , and for this setup,  $\Delta_{\text{NL}} = 0.06$  at the peak. Therefore, the nonlinear effects are weakly important for this situation.

The upper panel of Fig. 5 shows the value of the field at the peak,  $\varphi_{\text{peak}} := \sup[\varphi]$ , and the lower panel shows the position  $r_*^{(\text{peak})}$  of the peak with respect to the tortoise coordinate  $r_*$  as functions of  $t/M$ . The value of  $\varphi_{\text{peak}}$  oscillates with the period of about  $700M$ . The position of the peak also moves back and forth, and  $\varphi_{\text{peak}}$  increases when  $r_*^{(\text{peak})}$  decreases, i.e., when the peak location approaches the horizon. Therefore, the change in the amplitude is mainly caused not by the superradiant instability but by the change of the peak position. Namely, when the peak position approaches the horizon due to nonlinear interaction, the field gets compacted in a small region around the BH, and therefore, the field is amplified because of the energy conservation.

Figure 6 shows the energy flux  $F_E := d(\Delta E)/dt$  and the angular momentum flux  $F_J := d(\Delta J)/dt$  toward the horizon evaluated at  $r_* = -100M$ , where  $\Delta E$  and  $\Delta J$  are integrated fluxes defined in Eq. (2.12). Initially, both  $F_E$  and  $F_J$  are negative, reflecting the fact that we have chosen the  $(\ell, m) = (1, 1)$  mode of the

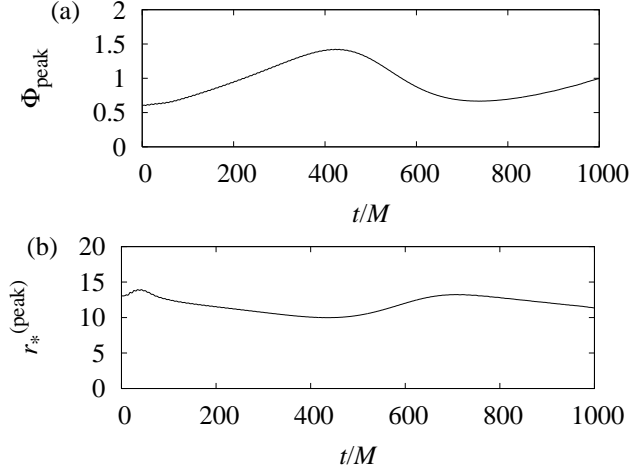


Fig. 5. The peak value  $\varphi_{\text{peak}}$  of the field  $\varphi$  (upper panel) and its location  $r_*^{(\text{peak})}$  with respect to the tortoise coordinate (lower panel) as functions of time observed in simulation (A) [i.e.,  $\varphi_{\text{peak}}(0) = 0.6$ ]. The peak location moves back and forth periodically. When the peak location becomes close to the horizon, the value of  $\varphi_{\text{peak}}$  becomes larger.

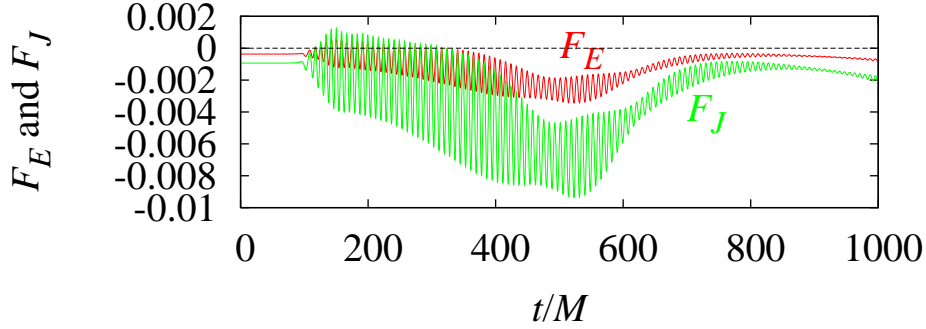


Fig. 6. Fluxes  $F_E$  and  $F_J$  of energy and angular momentum, respectively, toward the horizon observed in simulation (A) [i.e.,  $\varphi_{\text{peak}}(0) = 0.6$ ].  $F_E$  and  $F_J$  are negative except for very short periods. Therefore, the energy and angular momentum are extracted from the BH. The nonlinear effect makes their values larger.

superradiant bound state as the initial condition. The nonlinear effect appears at  $t/M \gtrsim 100$ . In that period, both  $F_E$  and  $F_J$  oscillate rapidly, and their mean values are negative. The absolute values of  $F_E$  and  $F_J$  become larger around  $t = 500M$ . The primary nonlinear effects are the following two. The first effect is that it enhances the amplitude of the waves of the  $(\ell, m) = (1, 1)$  mode that fall into the BH scarcely changing the real part of the frequency  $\omega_0$ . The second effect is that it generates waves of the  $(\ell, m) = (1, -1)$  mode with frequency  $\omega_{\text{NL}}$  which is approximately same as that of waves of the  $(\ell, m) = (1, 1)$  mode,  $\omega_{\text{NL}} \approx \omega_0$ . Although waves of the  $(\ell, m) = (1, -1)$  mode generate the positive energy flux to the horizon, it is very small in this case. Therefore, the first effect is much stronger than the second effect, and the rates of the extraction of energy and angular momentum are

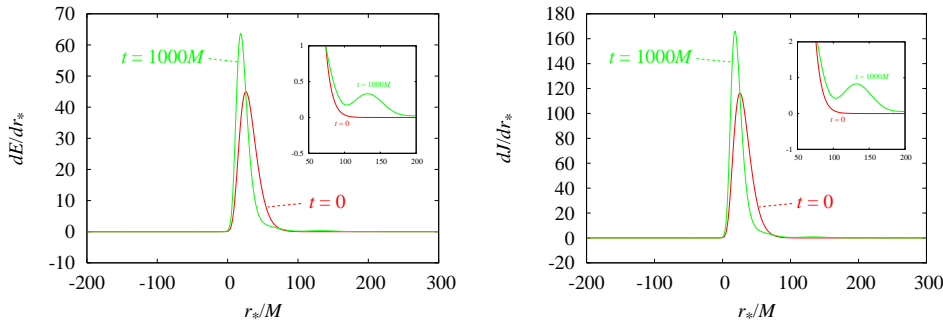


Fig. 7. The energy density  $dE/dr_*$  (left) and the angular momentum density  $dJ/dr_*$  (right) with respect to the tortoise coordinate  $r_*$  at time  $t/M = 0$  and 1000 for simulation (A) [i.e.,  $\varphi_{\text{peak}}(0) = 0.6$ ].

enhanced. By the interference of the two modes, the small oscillation of  $F_E$  and  $F_J$  appear with frequency  $\approx 2\omega_0$ . The generation of waves of the  $(\ell, m) = (1, -1)$  mode becomes more significant in the strongly nonlinear case [the simulation (B)] as explained later. Although the generation of the  $(\ell, m) = (1, -1)$  mode may seem strange because naively we expect the nonlinearity to produce modes in proportion to  $e^{\pm in(m\phi - \omega t)}$  with integer  $n$  from  $\text{Re}[e^{i(m\phi - \omega t)}]$ , the Green's function analysis in Appendix A supports it (see also Sec. 4.2.2).

The left and right panels of Fig. 7 show the energy density  $dE/dr_*$  and the angular momentum density  $dJ/dr_*$  with respect to the tortoise coordinate  $r_*$ , respectively, at  $t/M = 0$  and 1000. There are two peaks for the curve of  $t/M = 1000$  in each panel, the first peak near the horizon and the second peak at  $r_*/M \simeq 140$  (as can be seen in the inset). The locations of the first peaks of energy and angular momentum densities are shifted to small  $r_*$  values compared to  $t = 0$ . This means that most of the energy gets squeezed into a small region close to the horizon because of the nonlinear attractive self-interaction. Another effect of the nonlinearity is that it transports a small fraction of energy and angular momentum to a region far from the BH, making the small second peak as seen in the inset of each panel.

#### 4.2.2. Simulation (B): A strongly nonlinear case

In the simulation (B), we choose the initial amplitude to be  $\varphi_{\text{peak}}(0) = 0.7$ . The parameter  $\Delta_{\text{NL}} \simeq \varphi^2/6$  for the effect of the nonlinearity is  $\Delta_{\text{NL}} \simeq 0.082$  at the peak for this setup, and therefore, the nonlinear effect is larger compared to the simulations (A). The nonlinearity in this situation is strong enough for causing the bosenova collapse.

First, we would like to present some snapshots. Figure 8 shows the density plots of the axion field  $\varphi$  in the equatorial  $(r \cos \phi, r \sin \phi)$ -plane ( $\theta = \pi/2$ ) at  $t/M = 0, 150, 300,$  and  $450$ . The initial condition  $t = 0$  is the bound state of the Klein-Gordon field. In the time evolution, the axion cloud rotates counterclockwise and gradually becomes closer to the BH ( $t = 150$ ). At  $t = 300$ , the axion cloud is highly concentrated in a small region around the BH, and this is when the bosenova begins to happen. During the bosenova, the shape of the axion cloud becomes distorted

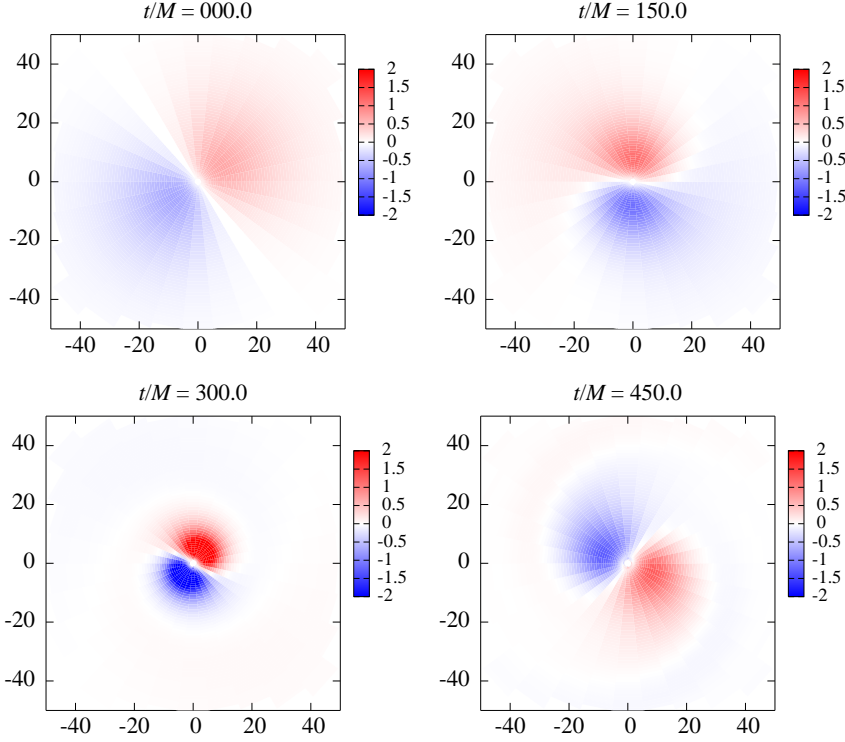


Fig. 8. Snapshots of density plot of the axion field  $\varphi$  in the equatorial ( $r \cos \phi, r \sin \phi$ )-plane ( $\theta = \pi/2$ ) at  $t/M = 0, 150, 300$ , and  $450$ . The axion cloud is rotating counterclockwise.

and part of the cloud is scattered to the distant region and into the BH ( $t = 450$ ).

The upper panel of Fig. 9 shows the value of the field at the peak  $\varphi_{\text{peak}} = \sup[\varphi]$ , and the lower panel shows the position of the peak with respect to the tortoise coordinate  $r_*$  as functions of  $t/M$ . In contrast to the case (A), the value of  $\varphi_{\text{peak}}$  increases only once around  $t = 300M$ , and after that it fluctuates with short periods. The position of the peak  $r_*^{(\text{peak})}$  also approaches the horizon only once, and after that, it fluctuates around  $r_* = 10M$  which is still fairly close to the horizon.

In order to understand the properties of the bosonova collapse, let us look at the field configuration focusing attention to the near horizon region. The left panel of Fig. 10 shows the density plot of the axion field  $\varphi$  at  $t = 500M$  in the  $(r_*/M, \phi)$  plane. The main part of the axion cloud is moving in the  $+\phi$  direction. During the bosonova, ingoing waves that are different from those of the bound state of the  $(\ell, m) = (1, 1)$  mode are continuously generated from the cloud, as can be clearly seen in this figure. The cloud remains around  $r_* \simeq 10M$ , while the waves fall into the BH. The generated waves are of the  $(\ell, m) = (1, -1)$  mode in spite of the fact that the initial condition has just the  $(\ell, m) = (1, 1)$  mode. The generated waves have wavelength  $\lambda_{\text{NL}} \simeq 8M$  in the tortoise coordinate  $r_*$ . This indicates  $\tilde{\omega}_{\text{NL}} \simeq 0.785M$  where  $\tilde{\omega} := \omega - m\Omega_H$  (see review in Sec. 2.2), and because the waves are in the  $m = -1$  mode, their angular frequency is  $\omega_{\text{NL}} \simeq 0.35/M$ . This angular frequency is approximately same



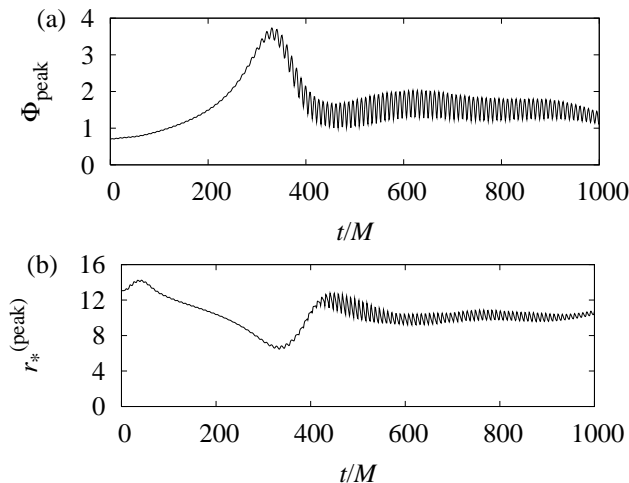


Fig. 9. Same as Fig. 5 but for simulation (B) [i.e.,  $\varphi_{\text{peak}}(0) = 0.7$ ]. The peak location  $r_*^{(\text{peak})}$  becomes fairly close to the horizon around  $t \simeq 350M$ , where  $\varphi_{\text{peak}}$  reaches approximately four. This is when the bosenova begins to happen, and the behavior after that time is very different from (A):  $r_*^{(\text{peak})}$  continues small oscillation around  $r_* = 10M$  with a short period, and correspondingly,  $\varphi_{\text{peak}}$  fluctuates around 1.5.

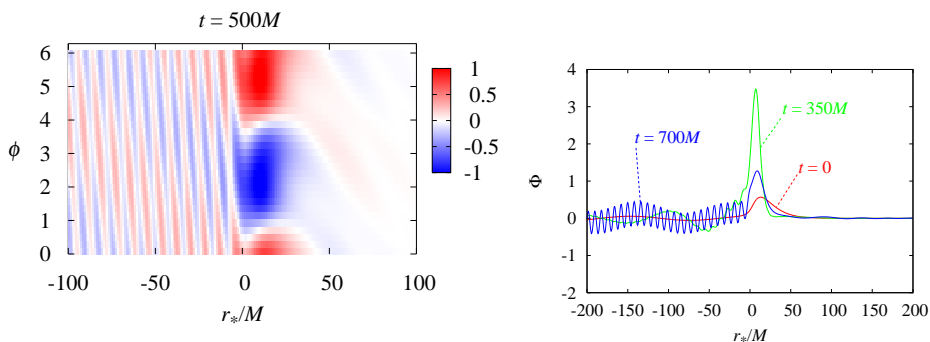


Fig. 10. Left panel: A snapshot of the field in the equatorial plane  $\theta = \pi/2$  at  $t = 500M$ . Here, the magnitude of the field  $\varphi$  is shown by density plot in the plane  $(r_*/M, \phi)$ . Right panel: Snapshots of the field  $\varphi$  as a function of  $r_*/M$  at  $\phi = 0$  in the equatorial plane  $\theta = \pi/2$  for  $t/M = 0, 350$ , and  $700$ .

as that of the bound state of the Klein-Gordon field,  $\omega_0 \simeq 0.39/M$ . Since those waves violate the superradiant condition  $\omega < m\Omega_H$  because  $m$  is negative, it carries the positive energy toward the horizon.

It is obvious that the generated ingoing waves originate from the nonlinear effect. However, at first glance, the generation of waves of the  $(\ell, m) = (1, -1)$  mode seems strange, because the nonlinear term  $\sim \varphi_0^3 \sim e^{3i(\phi - \omega_0 t)}$  is unlikely to generate the observed waves whose behavior is  $\sim e^{i(\phi + \omega_{\text{NL}} t)}$ . In Appendix A, we study the generation of waves by the nonlinear effect using the Green's function approach, and find that waves of the  $(\ell, m) = (1, -1)$  mode actually can be generated. Therefore,

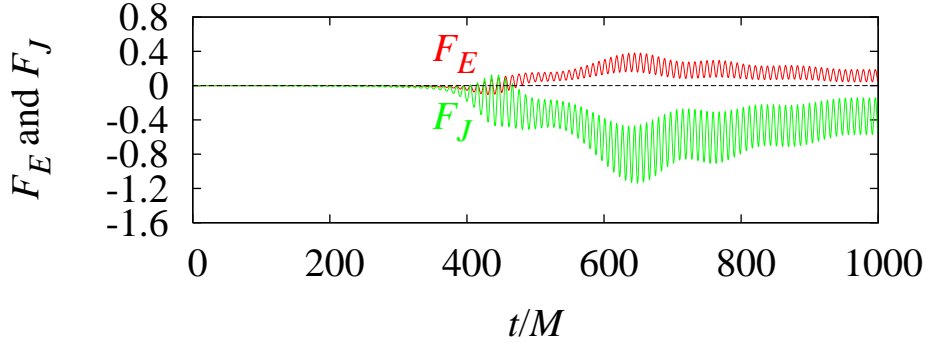


Fig. 11. Same as Fig. 6 but for simulation (B) [i.e.,  $\varphi_{\text{peak}}(0) = 0.7$ ]. After the bosenova happens at  $t \simeq 350M$ , the energy flux  $F_E$  to the horizon is always positive while the angular momentum flux  $F_J$  is negative. Therefore, the energy extraction stops while the angular momentum extraction continues.

the waves of the  $(\ell, m) = (1, -1)$  mode found in our simulation are not numerical artifact. In short, due to the nonlinear effect, several modes of the bound states (discussed in Sec. 2.2) of frequency  $\omega \approx \pm\omega_0$  are excited, and these modes include the modes with negative frequency. Since the  $(\ell, m) = (1, 1)$  mode of negative frequency is equivalent to the  $(\ell, m) = (1, -1)$  mode of positive frequency, waves of the  $(\ell, m) = (1, -1)$  mode can be observed.

The right panel of Fig. 10 shows the snapshots of the field on the  $\phi = 0$  line on the equatorial plane  $\theta = \pi/2$ , at time  $t/M = 0, 350$ , and  $700$ . At  $t/M = 350$ , the peak of the field becomes very high, and around this time, the bosenova begins to happen. At  $t/M = 700$ , the nonlinear generation of waves of  $(\ell, m) = (1, -1)$  mode continues, and the ingoing waves can be seen for  $r_* \lesssim 0$ .

Figure 11 shows the energy flux  $F_E$  and the angular momentum flux  $F_J$  toward the horizon evaluated at  $r_* = -100M$ . Although both  $F_E$  and  $F_J$  are negative initially, after the bosenova happens, the value of  $F_E$  becomes positive at least up to  $t = 1000M$ . Here, the dominant contribution to the flux comes from the waves of the  $(\ell, m) = (1, -1)$  mode generated by the nonlinear effect. Because those waves obviously violate the superradiant condition  $\omega < m\Omega_H$ , the energy flux toward the horizon becomes positive. As a result, the extraction of energy is prevented by the bosenova in this simulation, and about 5.3% of energy falls into the BH by  $t/M = 1500$ . On the other hand, the value of  $F_J$  continues to be negative, and the waves continue to extract the angular momentum from the BH. This is because the ingoing waves are in the  $m = -1$  mode, and hence, carry negative angular momentum if energy is positive. The small fluctuations of  $F_E$  and  $F_J$  come from the interference of the  $(\ell, m) = (1, \pm 1)$  modes, and the typical angular frequency of this oscillation is  $\approx 2\omega_0$ , similarly to the simulation (A).

The left and right panels of Fig. 12 show the energy density  $dE/dr_*$  and the angular momentum density  $dJ/dr_*$  with respect to the tortoise coordinate  $r_*$ , respectively, at  $t/M = 0, 750$ , and  $1500$ . At late time, most of the energy is contained in the domain  $0 \lesssim r_*/M \lesssim 30$ , and the energy and angular momentum densities

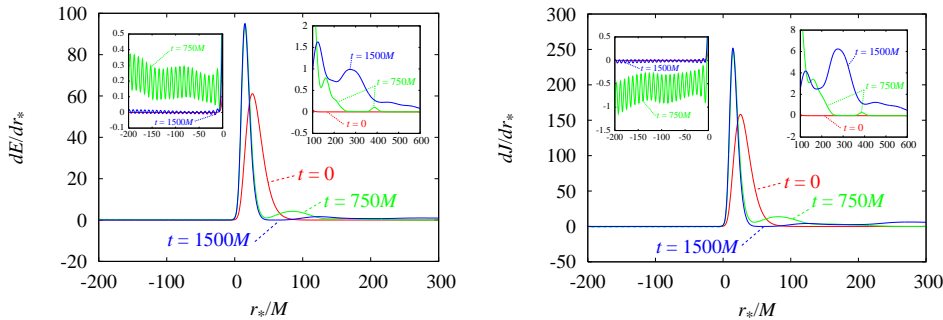


Fig. 12. The energy density  $dE/dr_*$  (left) and the angular momentum density  $dJ/dr_*$  (right) with respect to the tortoise coordinate  $r_*$  at time  $t/M = 0, 750$ , and  $1500$  for simulation (B) [i.e.,  $\varphi_{\text{peak}}(0) = 0.7$ ].

have similar shapes for  $t/M = 750$  and  $1500$ . The difference between  $t/M = 750$  and  $1500$  can be seen in the domains  $r_*/M \lesssim 0$  and  $r_*/M \gtrsim 100$ . The behavior of each of  $dE/dr_*$  and  $dJ/dr_*$  in the domain  $r_*/M \lesssim 0$  can be seen in the left inset of each panel. At  $t = 750M$ , the energy density is positive and the angular momentum density is negative. This is consistent with the fact that the energy and angular momentum fluxes to the horizon are positive and negative, respectively, as seen in Fig. 11. At  $t = 1500M$ , both two densities fluctuate around zero, and the mean values of energy and angular momentum densities are still positive and negative, respectively. This is because the nonlinear resonance becomes weak at this time, and the system settles down to a quasistationary state again. The behavior of each of  $dE/dr_*$  and  $dJ/dr_*$  at the distant place is shown in the right inset of each panel. At  $t = 750M$ , some fraction of energy and angular momentum are distributed at a far region. Around  $r_* = 400M$ , a small bump can be seen. This bump moves outward approximately at the speed of light. Therefore, a kind of “explosion” happens in the bosenova. However, this explosion is very small because this bump has only  $\approx 0.2\%$  of the total energy. At  $t = 1500M$ , more amount of energy and angular momentum can be seen at the distant place. Therefore, following the small explosion, the field energy gradually spreads out to the distant region. At  $t/M = 1500$ , about  $16.6\%$  of the total energy distributes in the region  $r_*/M \geq 60$ . Except for the small bump moving at the speed of light, all field in the distant region seems to be gravitationally bounded. The simulation was performed up to  $t/M = 2000$ , and it was found that after  $t/M = 1500$ , some part of the energy at the distant place begins to fall back.

It is interesting to study how much energy of the axion field is converted from the  $(\ell, m) = (1, 1)$  mode to other modes. Unfortunately, numerical decomposition of the field  $\varphi$  into the modes is rather tedious because it requires Fourier transform from the time domain to the frequency domain, and also, in the case of the Kerr spacetime, the separation constant and the spheroidal harmonics depend on the frequency  $\omega$ . Instead, we give rough estimate on how much energy is converted to the  $(\ell, m) = (3, \pm 3)$  mode in an approximate way. In this approximation, we use the spherical harmonics instead of the spheroidal harmonics, and decompose the field into

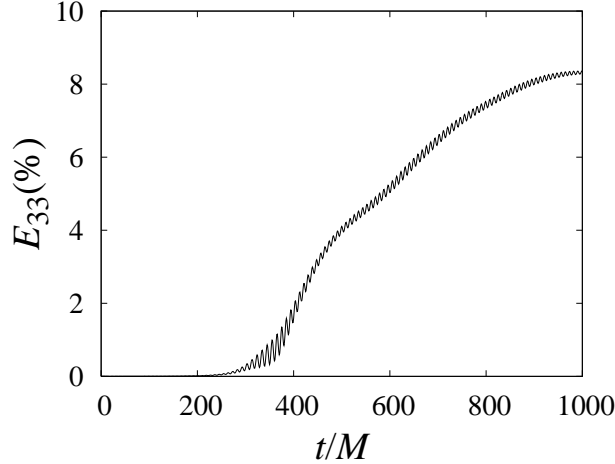


Fig. 13. The estimated amount of energy  $E_{33}$  of  $(\ell, m) = (3, \pm 3)$  mode generated by the mode mixing in the bosonova as a function of time  $t/M$ . Here  $E_{33}$  is normalized by the total energy  $E$  and shown in the unit of %. About 10% energy is converted into the  $(\ell, m) = (3, \pm 3)$  mode.

the form  $\varphi = \sum_{0 \leq m \leq \ell} \varphi_{\ell m}$ , where  $\varphi_{\ell m} := f_{\ell m}(t, r)Y_{\ell m}(\theta, \phi) + f_{\ell - m}(t, r)Y_{\ell - m}(\theta, \phi)$ . The energy  $E_{\ell m}$  of each  $(\ell, \pm m)$  mode is estimated by substituting  $\varphi_{\ell m}$  into the formula for the energy. In this manner, we have studied the mode  $0 \leq l \leq 4$ , and found that the modes with  $(\ell, m) = (1, \pm 1)$ ,  $(3, \pm 1)$ , and  $(3, \pm 3)$  are nonzero and the other modes are approximately zero.

Figure 13 shows the value of energy of the  $(\ell, m) = (3, \pm 3)$  mode normalized by the total energy,  $E_{33}/E$ , as a function of time. After the bosonova happens, the  $(\ell, m) = (3, \pm 3)$  mode starts to grow and has about 10% of the total energy at  $t/M = 1000$ . On the other hand, before the bosonova, the mode mixing is fairly weak, and almost all fields are in the  $(\ell, m) = (1, 1)$  mode. We evaluated the value of  $E_{33}/E$  also for the simulation (A) [i.e.,  $\varphi_{\text{peak}}(0) = 0.6$ ], and found that the  $(\ell, m) = (3, \pm 3)$  mode has at most 0.014% of the total energy. This result shows that the bosonova converts relatively large amount of the axion field from the  $(\ell, m) = (1, 1)$  mode to other modes.

To summarize, if the initial amplitude is sufficiently large, the bosonova happens for the axion cloud of quasibound state of the  $(\ell, m) = (1, 1)$  mode. The bosonova in this system is characterized by the following features. First, a small amount ( $\approx 0.2\%$ ) of energy comes out from the axion cloud approximately at the speed of light. After that, about 15% of energy gradually spreads out to the distant region, although it seems to be gravitationally bounded. Therefore, the bosonova of the BH-axion system is somewhat similar to the bosonova of BEC in experiments (In Sec. 6, we give a more detailed comparison). Second, about 5% of energy falls into the BH after the bosonova. This energy is carried by waves of the  $(\ell, m) = (1, -1)$  mode generated by the nonlinear effect. Therefore, in the BH-axion system, the “explosion” happens both to distant place and to the horizon. Finally, once the bosonova happens, the mode mixing effectively occur. In addition to the generation

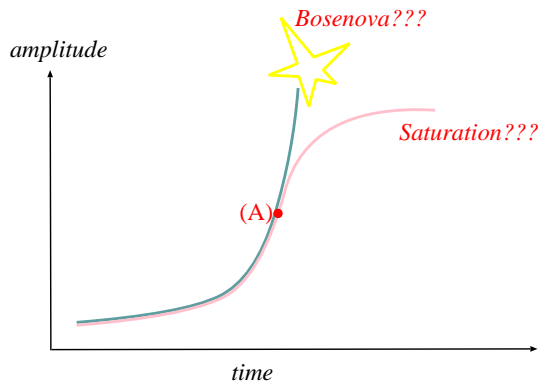


Fig. 14. Schematic picture of time evolution of the field amplitude and two possibilities of the final state of the superradiant instability.

of the  $(\ell, m) = (1, -1)$  mode, the  $\ell = 3$  mode was observed to get  $\approx 10\%$  of the total energy after the bosenova.

#### 4.3. Does the bosenova really happen?

In the two simulations performed above, we found the following: In the simulation (A), when the initial peak value is small, the nonlinear effect causes periodic changes in the peak location and the peak value, and enhances the energy and angular momentum extractions; In the simulation (B), when the initial peak value is large, the nonlinear effect causes an explosion, the bosenova. During the bosenova, waves of the  $(\ell, m) = (1, -1)$  mode violating the superradiant condition are generated, and thus, the energy flux toward the horizon becomes positive terminating the superradiant instability.

In this subsection, we discuss whether the bosenova happens as the result of the superradiant instability. In a realistic system, as the rotational energy of the BH is extracted, the field gradually gets amplified. In this sense, the simulation (B) may be artificial because we gave a quasibound state of large amplitude by hand and its initial condition may not be realized as the result of the superradiant instability. In particular, we have to take care of the possibility that the bosenova does not happen, as there are a lot of examples of nonlinear systems in which the nonlinear effects saturate the instabilities leading the systems to quasistable states. Figure 14 is a schematic picture depicting the two possibilities of time evolution: the bosenova and the saturation.

In order to discuss which is the case, we perform supplementary simulations as follows. In these simulations, we prepare the initial condition by applying the scale transformation to the result of the simulation (A) at  $t = 1000M$  as  $\varphi(0) = C\varphi^{(A)}(1000M)$  and  $\dot{\varphi}(0) = C\dot{\varphi}^{(A)}(1000M)$ . This is because in the presence of the nonlinear term, the energy gets confined in a smaller region near the BH compared to the case of the quasibound state of the massive Klein-Gordon field as found in Fig. 7, and the initial condition prepared by this procedure is expected to be more realistic and to approximate the nearly final state of the superradiant instability.

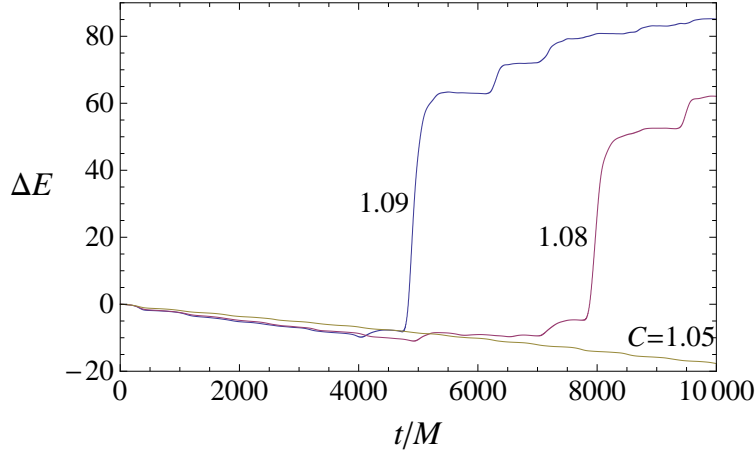


Fig. 15. The relation between time  $t$  and the amount of energy  $\Delta E$  that has fallen into the BH by the time  $t$ . Here, the cases of  $C = 1.05$ ,  $1.08$ , and  $1.09$  are shown.

The cases of  $C = 1.05$ ,  $1.08$ , and  $1.09$  were simulated. Here, the initial state for a larger  $C$  is expected to approximate the later state of Fig. 14.

Figure 15 shows the relation between time  $t$  and the amount energy  $\Delta E$  that has fallen by the time  $t$ . In other words,  $\Delta E$  is the integrated energy flux toward the horizon from time zero to  $t$ :  $\Delta E := \int_0^t F_E dt$ . The gradient of each curve shows the flux  $F_E$  toward the horizon: If it is negative (resp. positive), the negative (resp. positive) energy is falling into the BH. The curve of the case  $C = 1.05$  is always negative, and at this stage, the energy continues to be extracted. In this case, the averaged rate of the superradiant instability is  $\gamma_{\text{NL}} M \approx 5.85 \times 10^{-7}$ , which is larger than that of the case of the linear Klein-Gordon field,  $\gamma M = 1.30 \times 10^{-7}$ . This confirms that the nonlinear effect enhances the rate of superradiant instability before the bosenova. The bosenova does not happen at least by time  $t/M = 10000$ .

Next, let us look at the case  $C = 1.09$ . In this case, the value of  $F_E$  is negative until  $t/M \simeq 4000$ . Here, the rate of energy extraction is  $\gamma_{\text{NL}} M \simeq 7.45 \times 10^{-7}$ , which is further larger than that of the case  $C = 1.05$ . However, around  $t/M \simeq 4000$ , the value of  $F_E$  becomes positive, and for  $t/M \gtrsim 4500$ , the value of  $F_E$  becomes positive and fairly large: the bosenova happens around this time. This case represents the example such that the bosenova happens after a certain period of energy extraction. Therefore, it is natural to consider that this simulation approximates what actually happens at the final stage of the superradiant instability. The burst of positive energy toward the horizon continues until  $t/M \simeq 5300$ , and after that small explosions happen intermittently.

In the case of  $C = 1.08$ , the energy extraction continues from  $t/M = 0$  to  $5000$ . Around  $t/M = 5000$  and  $7500$ , small amounts of positive energy fall into the BH, and then, around  $t/M = 8000$ , a large positive ingoing energy flux is generated. This is the bosenova in this case. The bosenova in the case  $C = 1.08$  happens later than the case  $C = 1.09$ , mainly because the initial amount of energy of the former is smaller than that of the latter, and therefore, a longer period of energy extraction is

required. However, it should be noted that the bosenova of these two cases happen at different values of energy: The amount of energy when the positive flux is first generated is  $E/[(f_a/M_p)^2 M] \simeq 1633$  and  $1607$  for the cases  $C = 1.09$  and  $1.08$ , respectively. Although the criterion for the occurrence of the bosenova is mainly determined by the energy amount, it would depend also on the detailed structure of the axion cloud.

The natural picture of the final stage of the superradiant instability is as follows. Before the bosenova, similarly to the case of  $C = 1.05$ , the energy continues to be extracted and the rate of the energy extraction is gradually enhanced. Then, at a certain critical point, where the energy of the axion cloud is  $E/[(f_a/M_p)^2 M] \approx 1620$ , a large amount of positive energy suddenly falls into the BH, and here, the bosenova happens like the simulations of  $C = 1.08$  and  $1.09$ . The answer to the question “Does the bosenova really happen?” is “Yes,” because from our simulations, it is natural to consider that the bosenova actually happens as a result of the superradiant instability. In particular, we have obtained no evidence for the possibility that the nonlinear effect saturates the growth by the superradiant instability and leads the system to a quasistable state.

If we assume the decay constant  $f_a$  to be the GUT scale,  $\approx 10^{16}\text{GeV}$ , the bosenova collapse happens when the energy of the axion cloud grows to be  $E \simeq 1.6 \times 10^{-3}M$ , i.e., when the axion cloud gets energy of  $\approx 0.16\%$  of the BH mass. Therefore, if the value of  $f_a$  is the GUT scale or smaller, the back reaction to the background spacetime, such as the change in the parameter in  $M$  and  $a$  of the BH or the distortion of the background geometry by the axion cloud, is negligible. On the other hand, if we assume  $f_a \approx 10^{17}\text{GeV}$ , the bosenova collapse happens when  $E \simeq 0.16M$ , i.e., when the axion cloud gets energy of  $\approx 16\%$  of the BH mass. In such a situation, back reaction to the background geometry is significant, and the bosenova phenomena has to be studied by the method of numerical relativity.

The time evolution long after the bosenova is also an interesting subject, although this is beyond the scope of this paper. Looking at Fig. 15, in the case of  $C = 1.09$ , the small amount of positive energy intermittently falls into the BH. One possibility is that this phenomena continues and the axion cloud continue to extract and lose small amounts of energy. Another possibility is that the axion cloud loses almost all energy, and the superradiant instability happens from the beginning, leading to the bosenova collapse that has approximately same scale as the previous one. In order to clarify which is the case, a very-long-term simulation or construction of a good approximate model is necessary.

When we consider a very-long-term evolution of the BH-axion system, taking account of changes in mass  $M$  and angular momentum  $J$  of the BH is also important. In our simulations, the energy is extracted from the BH in superradiant instability and falls back to the BH in the bosenova collapse. On the other hand, the angular momentum is extracted both in the superradiant instability and in the bosenova collapse. Therefore, the spin parameter  $a/M$  would gradually decrease in a very-long-term evolution. As a result, superradiant instability of the  $(\ell, m) = (1, 1)$  mode will stop when  $a/M$  is decreased to a certain value that is determined by the mass  $\mu$  of the axion (see Fig. 7 of Ref. 26)). After that, superradiant instability of the

$(\ell, m) = (2, 2)$  mode will become a primary factor in determining the evolution of the axion cloud.

### §5. Effective theory of axion cloud model

In this section, we discuss the reason why the bosenova happens in the BH-axion system by introducing an effective theory for this system. In this discussion, we model the axion cloud using a time-dependent Gaussian wavefunction. Also, we assume the non-relativistic approximation in which the gravity is treated by the Newtonian potential. The distribution is specified by the following three parameters:  $\delta_r$  (the width of the wavepacket along the  $r$  direction),  $\delta_\nu$  (the width along the  $\theta$  direction), and  $r_p$  (the position of the peak with respect to the  $r$  coordinate). Under these approximations, we derive the effective action for the three parameters and find various properties of the bosenova which are consistent with the simulations.

#### 5.1. Effective action

The action for the axion field  $\Phi$  is given by Eq. (2.1). In terms of the normalized field  $\varphi = \Phi/f_a$ , the action is rewritten as

$$\hat{S} = \int d^4x \sqrt{-g} \left[ -\frac{1}{2}(\nabla\varphi)^2 - \mu^2 \left( \frac{\varphi^2}{2} + \hat{U}_{\text{NL}}(\varphi) \right) \right], \quad (5.1)$$

where the nonlinear potential  $\hat{U}_{\text{NL}}$  is defined by

$$\hat{U}_{\text{NL}}(\varphi) = 1 - \frac{\varphi^2}{2} - \cos\varphi = -\sum_{n=2}^{\infty} \frac{(-1)^n}{(2n)!} \varphi^{2n}. \quad (5.2)$$

We introduce  $\psi$  as

$$\varphi = \frac{1}{\sqrt{2\mu}} (e^{-i\mu t} \psi + e^{i\mu t} \psi^*). \quad (5.3)$$

Here,  $\psi$  is a slowly varying function under the non-relativistic approximation. Substituting this formula into Eq. (5.1), we have

$$\hat{S}_{\text{NR}} = \int d^4x \left[ \frac{i}{2} (\psi^* \dot{\psi} - \dot{\psi} \psi^*) - \frac{1}{2\mu} \partial_i \psi \partial_i \psi^* + \frac{\alpha_g}{r} \psi^* \psi - \mu^2 \tilde{U}_{\text{NL}}(|\psi|^2/\mu) \right], \quad (5.4)$$

where  $\alpha_g := M\mu$  and

$$\tilde{U}_{\text{NL}}(x) = -\sum_{n=2}^{\infty} \frac{(-1/2)^n}{(n!)^2} x^n. \quad (5.5)$$

Here, the Newtonian approximation is adopted for gravity.

Now, we assume the form of  $\psi$  as

$$\psi = A(t, r, \nu) e^{iS(t, r, \nu) + m\phi}, \quad (5.6)$$

where  $\nu := \cos\theta$  and we set  $m = 1$ . The functions  $A(t, r, \nu)$  and  $S(t, r, \nu)$  are chosen to be the following form:

$$A(t, r, \nu) \approx A_0 \exp \left[ -\frac{(r - r_p)^2}{4\delta_r r_p^2} - \frac{(\nu - \nu_p)^2}{4\delta_\nu} \right], \quad (5.7)$$



$$S(t, r, \nu) \approx S_0(t) + p(t)(r - r_p) + P(t)(r - r_p)^2 + \pi_\nu(t)(\nu - \nu_p)^2 + \dots \quad (5.8)$$

$\delta_r(t)$  is the width of the wavepacket along the  $r$  direction,  $\delta_\nu(t)$  is the width along the  $\nu$  direction (i.e.,  $\theta$  direction), and  $r_p(t)$  is the position of the peak with respect to  $r$  coordinate. Since the center of the wavepacket always exists on the equatorial plane, the peak position with respect to  $\nu$  coordinate is always zero,  $\nu_p \equiv 0$ . We define  $N$  as

$$N = \int d^3x A^2 \approx 4\pi^2 A_0^2 \sqrt{\delta_r \delta_\nu} r_p^3 (1 + \delta_r). \quad (5.9)$$

Here, we ignored the inner cutoff of the integration range of  $r$ . In a similar manner, we perform the integration of the action (with respect to spatial coordinates) and derive the Lagrangian density as

$$L = -\dot{S}_0 N + p\dot{r}_p N + (\dot{p} - 2P\dot{r}_p)2r_p \frac{\delta_r}{1 + \delta_r} N - \dot{P}r_p^2 \delta_r \frac{1 + 3\delta_r}{1 + \delta_r} N - \dot{\pi}_\nu \delta_\nu N - H \quad (5.10)$$

with

$$H = T + V, \quad (5.11)$$

where

$$T = \frac{N}{2\mu} \left[ p^2 + 8pPr_p \frac{\delta_r}{1 + \delta_r} + 4P^2 r_p^2 \delta_r \frac{1 + 3\delta_r}{1 + \delta_r} + 4\pi_\nu^2 \frac{\delta_\nu}{r_p^2 (1 + \delta_r)} \right] \quad (5.12)$$

$$\begin{aligned} \frac{V}{N\mu\alpha_g^2} &= \frac{1}{2(\alpha_g\mu r_p)^2(1 + \delta_r)} \left( 1 + \delta_\nu + \frac{1}{4\delta_r} + \frac{1}{4\delta_\nu} \right) - \frac{1}{(\alpha_g\mu r_p)(1 + \delta_r)} \\ &\quad - \alpha_g^{-2} \sum_{n=2}^{\infty} \frac{(-1/2)^n}{(n!)^2 n} \left[ \frac{N_*}{\sqrt{\delta_r \delta_\nu} (\alpha_g\mu r_p)^3 (1 + \delta_r)} \right]^{n-1}, \quad (5.13) \end{aligned}$$

with  $N_* = (\alpha_g^3 \mu^2 / 4\pi^2) N$ . Here, we have kept terms up to the first-order in  $\delta_\nu$  because the wavepacket form, Eq (5.7), is not a very good approximation in the  $\nu$  direction and taking account of higher-order terms in  $\delta_\nu$  does not have an important meaning. The term depending on  $\dot{S}_0$  can be omitted since it just gives the conservation of  $N$ . The variables  $p$ ,  $P$ , and  $\pi_\nu$  can be related to the conjugate momenta of the variables  $\delta_r$ ,  $\delta_\nu$ , and  $r_p$ , and therefore, we can express the Lagrangian only in terms of  $\delta_r$ ,  $\delta_\nu$ , and  $r_p$ , and their time derivatives. To summarize, the equivalent Lagrangian is

$$L = T - V, \quad (5.14)$$

$$T = \frac{1}{2} A \dot{\delta}_r^2 + B \dot{\delta}_r \dot{r}_p + \frac{1}{2} C \dot{r}_p^2 + \frac{1}{2} D \dot{\delta}_\nu^2, \quad (5.15)$$

where

$$A = \frac{1}{4} N \mu r_p^2 \frac{1 + 45\delta_r + 198\delta_r^2 + 126\delta_r^3 + 45\delta_r^4 + 9\delta_r^5}{(1 + \delta_r)^3 \delta_r (1 + 3\delta_r^2)}, \quad (5.16a)$$

$$B = \frac{1}{2} N \mu r_p \frac{-7 - 30\delta_r + 54\delta_r^2 + 30\delta_r^3 + 9\delta_r^4}{(1 + \delta_r)^2 (1 + 3\delta_r^2)}, \quad (5.16b)$$

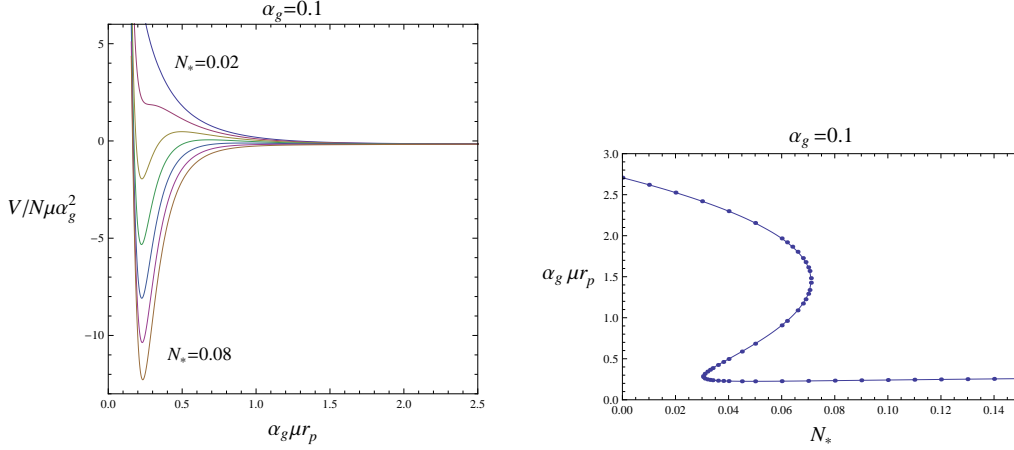


Fig. 16. Left panel: The behavior of the potential  $V$  as a function of  $\alpha_g\mu r_p$  for  $N_* = 0.02, \dots, 0.08$  with 0.01 intervals in the case  $\alpha_g = 0.1$ . There is one stable point for  $N_* = 0.02$ , and as  $N_*$  is increased, another stable point appears for  $N_* \approx 0.03$ . The outer stable point disappears for  $N_* \approx 0.07$  and the system moves to the inner stable point (i.e., the bosenova). For  $N_* = 0.08$ , there is only one stable point at  $\alpha_g\mu r_p \approx 0.025$ . Right panel: The position of the equilibrium point as a function of  $N_*$  in the case  $\alpha_g = 0.1$ . For  $0.0304 \lesssim N_* \lesssim 0.071$ , there are two stable points and one unstable point, while only one stable point exists for  $N_* \lesssim 0.0304$  and  $\gtrsim 0.071$ .

$$C = N\mu \frac{1 + 6\delta_r - 26\delta_r^2 + 18\delta_r^3 + 9\delta_r^4}{(1 + \delta_r)(1 + 3\delta_r^2)}, \quad (5.16c)$$

$$D = \frac{1}{4} N\mu r_p^2 \frac{(1 + \delta_r)}{\delta_\nu}. \quad (5.16d)$$

The potential  $V$  is given in Eq. (5.13).

## 5.2. Equilibrium point of the potential

Let us study the properties of the potential  $V$ . This potential is a function defined in the three-dimensional phase space  $(\delta_r, \delta_\nu, \alpha_g\mu r_p)$ . For each  $N_*$ , the equilibrium point is determined by  $V_{,\delta_\nu} = V_{,\delta_r} = V_{,r_p} = 0$ . From this equilibrium condition, the following two simple relations are obtained:

$$\delta_r = \frac{-1 + 4\delta_\nu^2 + \sqrt{1 - 8\delta_\nu + 8\delta_\nu^2 + 64\delta_\nu^3 + 16\delta_\nu^4}}{2(-2 + 4\delta_\nu + 16\delta_\nu^2)}, \quad (5.17)$$

$$\alpha_g\mu r_p = 4\delta_\nu - \frac{1}{2\delta_\nu} + \frac{1}{4\delta_r} + 1. \quad (5.18)$$

If we impose these two conditions (5.17) and (5.18), we have a line in the three-dimensional phase space  $(\delta_r, \delta_\nu, \alpha_g\mu r_p)$ , and along this line, the potential  $V$  can be regarded as the function of  $\alpha_g\mu r_p$ . Let us study the behavior of this function  $V(\alpha_g\mu r_p)$  varying the value of  $N_*$ . We also plot the value of  $\alpha_g\mu r_p$  at the equilibrium point as a function of  $N_*$ . In the following, the two cases  $\alpha_g = 0.1$  and  $0.4$  are shown.

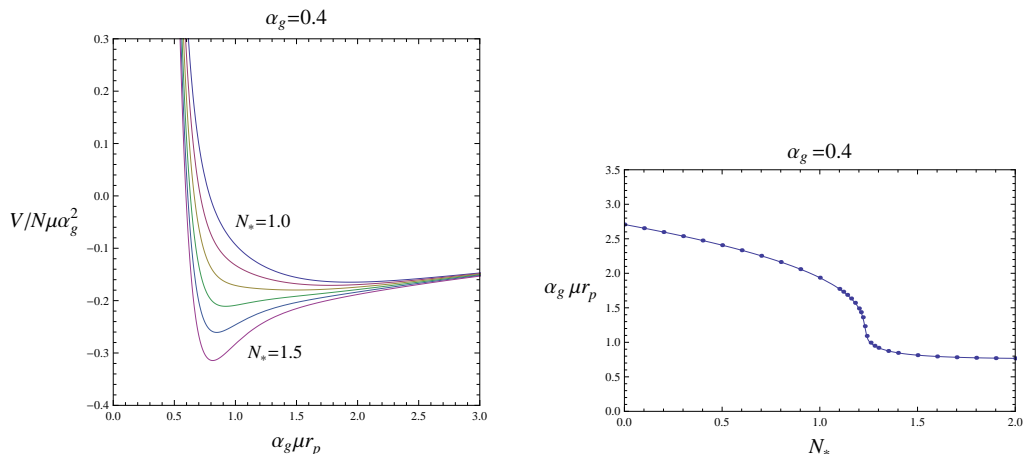


Fig. 17. The same as Fig. 16 but for  $\alpha_g = 0.4$ . The cases  $N_* = 1.0, \dots, 1.5$  are shown with 0.1 intervals for left panel. In this case, only one stable point exists for all  $N_*$ . Around  $N_* = 1.2$ , the position of the peak  $\alpha_g\mu r_p$  rapidly changes to a smaller value.

### 5.2.1. The case $\alpha_g = 0.1$

Let us look at the case  $\alpha_g = 0.1$ . The left panel of Fig. 16 shows the relation between  $\alpha_g\mu r_p$  and  $V$  along the line introduced above. The cases of  $N_* = 0.02, \dots, 0.08$  are depicted with 0.01 intervals. The right panel of Fig. 16 shows the relation between  $N_*$  and  $\alpha_g\mu r_p$  at the equilibrium point. For  $N_* < 0.0304$ , there is only one stable point. But as the  $N_*$  is increased, the situation changes: At  $N_* \simeq 0.0304$ , another stable point appears inside of the original stable point, and the two stable points exist for  $0.0304 \lesssim N_* \lesssim 0.071$ . At  $N_* \simeq 0.071$ , the outer stable point disappears, and only one stable point exists for  $N_* \gtrsim 0.071$ .

The interpretation of this result is as follows. Because of the superradiant instability, the value of  $N_*$  is gradually increased and the shape of the potential gradually changes. The position of the wavepacket is around  $\alpha_g\mu r_p \approx 2.7$  for small  $N_*$ , and it becomes smaller as  $N_*$  is increased. When  $N_*$  reaches  $\approx 0.03$ , a new stable point appears inside of the original stable point. The system remains at the original outer stable point for a while, i.e., until  $N_*$  reaches  $\approx 0.07$ . When  $N_*$  exceeds  $\approx 0.07$ , the outer stable point disappears, and therefore, the system jumps from the original outer stable point to the inner stable point. Accordingly, the value of  $\alpha_g\mu r_p$  jumps from  $\approx 1.5$  to  $\approx 0.25$ . So, the phase transition occurs when the amplitude reaches some critical point, and this is interpreted as the bosenova collapse. This is consistent with our simulation results: In simulation (A), the peak position continues to oscillate in relatively distant region, while in simulation (B), the peak position remains in the neighborhood of the horizon after the bosenova.

### 5.2.2. The case $\alpha_g = 0.4$

We turn our attention to the case  $\alpha_g = 0.4$ . The left panel of Fig. 17 shows the value of  $V$  as a function of  $\alpha_g\mu r_p$  along the line in the phase space  $(\delta_r, \delta_\nu, \alpha_g\mu r_p)$  introduced in the beginning of Sec. 5.2. The cases of  $N_* = 1.0, \dots, 1.5$  are depicted with 0.1 intervals. The right panel of Fig. 17 shows the relation between  $N_*$  and

$\alpha_g \mu r_p$  at the equilibrium point. In this case, there is only one stable point for all values of  $N_*$ . Around  $N_* \approx 1.2$ , the value  $\alpha_g \mu r_p$  of the equilibrium point rapidly decreases as  $N_*$  is increased, and hence, the equilibrium point becomes located closer to the horizon.

Our interpretation is as follows. In this axion cloud model, the phase transition does not occur for  $\alpha_g = 0.4$ : The situation with two stable equilibrium points occurs only for  $\alpha_g \lesssim 0.3$ . But in our simulations for  $\alpha_g = 0.4$ , the bosenova suddenly happens. Therefore, the phase transition seen in the  $\alpha_g = 0.1$  case gives a more correct picture. This discrepancy seems to arise because the axion cloud model discussed here is a model of rough approximation. Except for this point, however, the axion cloud model reproduces various characteristic features of the phenomena in the simulations. For example, Fig. 17 shows that as the superradiant instability progresses, the value of  $\alpha_g \mu r_p$  of the peak position becomes smaller, and around the ‘‘critical’’ value  $N_* \approx 1.2$ , the position rapidly becomes very close to the horizon. These are quite consistent with the results of our numerical simulations.

### 5.3. Small oscillations around the equilibrium point

It is also interesting to study small oscillations around the equilibrium point because it allows us to estimate the typical dynamical time scales of the BH-axion system. Here, we introduce the phase space parameter  $q_i$  defined by

$$q_i = (\delta_r, \delta_\nu, \alpha_g \mu r_p). \quad (5.19)$$

with  $i = 1, 2$ , and 3. The equilibrium position is denoted by  $q_i^{(0)}$  and the deviation  $\Delta q_i$  from the equilibrium point is introduced by  $q_i = q_i^{(0)} + \Delta q_i$ . Using the standard method in the classical mechanics, we can rewrite the Lagrangian in terms of  $\Delta q_i$  collecting only the second-order terms, and derive the equation of the harmonic oscillators,

$$\Delta \ddot{q}_i = -\Omega_{ij} \Delta q_j. \quad (5.20)$$

The solution of this equation can be written as a linear superposition of three normal modes, and their squared frequencies  $\omega_{\text{EG}}^2$  are given by the eigenvalues of the matrix  $\Omega_{ij}$ . For each value of  $\omega_{\text{EG}}^2$ , there exists an eigenvector describing the direction of oscillation of that normal mode in the phase space.

In the following, we discuss the cases  $N_* = 1.1$  and 1.3 for  $\alpha_g = 0.4$ . Because the bosenova happens around  $N_* \approx 1.2$ , the cases  $N_* = 1.1$  and  $N_* = 1.3$  are expected to approximate the state before and after the bosenova, respectively.

#### 5.3.1. The case $\alpha_g = 0.4$ and $N_* = 1.1$

In this case, the eigenvalues of the matrix  $\Omega_{ij}$  are given by

$$\left( \frac{\omega_{\text{EG}}}{\mu \alpha_g^2} \right)^2 = 1.141, 0.249, 0.0166, \quad (5.21)$$

with the corresponding eigenvectors

$$\Delta q_i = \begin{pmatrix} 0.110 \\ -0.027 \\ 0.994 \end{pmatrix}, \begin{pmatrix} 0.075 \\ 0.724 \\ 0.686 \end{pmatrix}, \begin{pmatrix} -0.378 \\ -0.005 \\ 0.925 \end{pmatrix}. \quad (5.22)$$

Let us focus attention to the third mode with  $(\omega_{\text{EG}}/\mu\alpha_g^2)^2 \simeq 0.0166$ . This mode represents the oscillation of the axion cloud in the direction of  $r$  and  $\delta_r$ , which scarcely changes the shape in the  $\nu$  direction. The period of the oscillation of this mode is

$$\Delta t \approx 761M. \quad (5.23)$$

This is consistent with the longterm oscillation found in the simulation (A) in Sec. 4.2.1. The origin of the long period of the oscillation is that the effective potential  $V(\alpha_g\mu r_p)$  becomes approximately flat and therefore the second-order derivative of this function becomes very small just before the bosenova happens.

5.3.2. The case  $\alpha_g = 0.4$  and  $N_* = 1.3$

In this case, the eigenvalues of the matrix  $\Omega_{ij}$  are

$$\left(\frac{\omega_{\text{EG}}}{\mu\alpha_g^2}\right)^2 = 14.06, 5.59, 0.175, \quad (5.24)$$

with the eigenvectors

$$\Delta q = \begin{pmatrix} 0.218 \\ -0.030 \\ 0.975 \end{pmatrix}, \begin{pmatrix} 0.070 \\ 0.927 \\ 0.367 \end{pmatrix}, \begin{pmatrix} -0.640 \\ -0.085 \\ 0.763 \end{pmatrix}. \quad (5.25)$$

Each eigenvalue in the case  $N_* = 1.1$  is larger than the corresponding eigenvalue in the case  $N_* = 1.3$ . The period of oscillation of the first mode is

$$\Delta t \approx 26M. \quad (5.26)$$

Although this period is longer than the period  $\Delta t \approx 10M$  observed in simulation (B) in Sec. 4.2.2, this model explains that the typical dynamical time scale after the bosenova becomes shorter compared to that before the bosenova. The discrepancy would be because the axion cloud model discussed here is a rough approximate model; If this model is improved so that the two stable equilibrium positions appear also for  $\alpha_g = 0.4$ , it would give shorter periods of oscillations.

## §6. Summary and discussion

In this paper, we have studied the sine-Gordon field in a Kerr spacetime motivated by landscape of axionlike particles/fields, i.e. the axiverse. In order to calculate the evolution of a scalar field in a Kerr spacetime, we developed a 3D code that has the ability to describe the growth rate by superradiant instability of the linear Klein-Gordon field with  $\lesssim 2\%$  error (Sec. 3.2.1). Using this code, we have performed simulations for the scalar field mass  $\alpha_g = M\mu = 0.4$  and the BH rotation parameter  $a/M = 0.99$  (Sec. 4.2), where the initial condition is taken to be the quasistationary bound state of the  $(\ell, m) = (1, 1)$  mode of the Klein-Gordon equation. When the initial peak value is small (Sec. 4.2.1), the nonlinear effect causes periodic changes in the peak location and the peak value, and the nonlinear effect enhances the energy and angular momentum extractions. On the other hand, if the initial peak value is

relatively large (Sec. 4.2.2), the nonlinear effect causes a collapse of the axion cloud and a subsequent explosion, i.e. the bosonova collapse. During the bosonova collapse, a kind of resonance occurs to generate waves of the  $(\ell, m) = (1, -1)$  mode falling into the BH. Since these waves violate the superradiant condition, the energy flux toward the horizon becomes positive. Therefore, the energy extraction is terminated by the bosonova.

In Sec. 4.3, we have discussed whether the bosonova happens or not as a result of the superradiant instability taking account of the two possibilities, the bosonova collapse and the saturation of the superradiant instability. We performed additional simulations from improved initial conditions that are expected to be more realistic. In these simulations (the cases  $C = 1.08$  and  $1.09$ ), the energy extraction continued for a long period of time and suddenly the bosonova collapse happened. This result supports the possibility that the bosonova collapse actually occurs as a result of the superradiant instability when the axion cloud gets energy of  $E \approx 1600(f_a/M_p)^2 M$  (for the present setup  $\alpha_g = 0.4$  and  $a/M = 0.99$ ). If the decay constant is order of the GUT scale,  $f_a \approx 10^{16}$  GeV, the energy at the bosonova collapse is 0.16% of the BH mass.

In Sec. 5, we have discussed why the bosonova happens by constructing an effective theory in the nonrelativistic approximation. The axion cloud is assumed to be a time-dependent Gaussian wavepacket, and the effective theory is described by dynamics of three variables that specify its shape. The dynamics is determined by a potential  $V$  whose behavior depends on the amplitude of the wavepacket. When the value of  $\alpha_g$  is small (e.g.,  $\alpha_g = 0.1$  in Sec. 5.2.1), there are two (outer and inner) stable minima in the potential  $V$  for a small amplitude, and the outer minimum disappear when amplitude grows to some value. Therefore, the bosonova collapse is explained by the phase transition from the outer stable point to the inner stable point. The effective theory also indicates that for large values of  $\alpha_g$ , such phase transition does not occur and the bosonova is unlikely to happen. The dynamical time scales observed in our simulations before and after the bosonova also can be successfully explained by studying small oscillations around the local minimum. Therefore, the axion cloud model describes the BH-axion system fairly accurately. This result indicates that the critical amplitude for the onset of the bosonova collapse is primarily determined by the self-interaction of axions rather than the nonlinear gravity of the BH, although the nonlinear BH gravity is important in making the field amplitude larger by extraction of the rotational energy of the BH.

Here, we compare the bosonova phenomena in the system of BEC atoms and in the BH-axion system. The action of the BH-axion system in nonrelativistic approximation, Eq. (5.4), has the same form as the action of the BEC atoms, e.g. Eq. (3) of Ref. 10), except that the parabolic potential is replaced by the Newton potential and the higher-order terms are included in the nonlinear potential. For this reason, the two phenomena are naturally expected to have similarity to each other. In fact, both of the growth of the amplitude in Fig. 9 in our simulation and the implosion of BEC atoms (e.g., Fig. 3 of Ref. 10) or Fig. 1 of Ref. 11)) are caused by nonlinear attractive interaction. But there exists qualitative difference between the two systems: The big implosions continue to happen in the BEC system, while

the big implosion happens only once in the BH-axion system. Also, the growth of the peak height in our system is not as sharp as the BEC system. The reason is that we are dealing with the  $(\ell, m) = (1, 1)$  mode while the typical BEC system is in the  $(\ell, m) = (0, 0)$  mode. Since the BEC system does not have the angular momentum, the BEC atoms concentrate to the center and the peak height can become large almost unboundedly, and this process can continue intermittently. On the other hand, since the axion cloud is rotating around the BH in our system, the centrifugal force prevents the axion cloud from collapsing to the center. For this reason, the growth of the peak height is limited. This point is also understood by looking at the effective potential. In Ref. 10), an effective theory for the BEC atoms was discussed using a time-dependent Gaussian wave function in a similar manner to Sec. 5. The effective potential of the BEC system behaves as  $f(0) = -\infty$ , and this enables the BEC atoms to concentrate at the center. On the other hand, the effective potential of the BH-axion system behaves as  $V(0) = \infty$ , and this makes the inner stable point. Hence, the high concentration of axion cloud to the center is prohibited. (Compare Fig. 1 of Ref. 10) and Fig. 16 of this paper.)

The authors of Ref. 9), 10), 11) discussed the fact that the bursts after the implosions in the BEC system are caused by the two-body dipolar and the three-body recombination of the BEC atoms. The loss of atoms causes the decrease in the attractive interaction, and the burst is generated by the zero-point kinetic pressure. In numerical simulations, the loss of atoms are handled by introducing the phenomenological terms  $(-i\hbar/2)(K_2|\psi|^2 + K_3|\psi|^4)\psi$  to the nonlinear Schrödinger equation (e.g., Eq. (1) of Ref. 11)). Although no such phenomenological terms are introduced in solving the axion field in our paper, part of the axion cloud was observed to spread out to the distant region. The reason would be that in the BH-axion system, infalling waves of the  $m = -1$  mode are generated by excitation of the bound states, causing the loss of energy (and therefore, the attractive interaction) of the axion cloud. Therefore, in our system, fall of a fraction of the axion cloud to the BH would play the same role as the three-body recombination of atoms in the BEC system.

Finally, we briefly discuss whether the bosenova can be observed by gravitational wave detectors. Studying gravitational waves emitted from an axion cloud is rather difficult since it requires quantum mechanical description, and the quadrupole formula cannot be directly applied (although the authors of Ref. 2) discussed the fact that the quadrupole formula corresponds to level transition of axion particles). The level transition from the  $(\ell, m) = (1, 1)$  mode is prohibited by the selection rule, and the two axion annihilation to a graviton is estimated to be rather small.<sup>2)</sup> Therefore, the gravitational wave emission from the axion cloud scarcely affects the occurrence of the bosenova. On the other hand, it would be possible to discuss gravitational waves emitted in the bosenova collapse by the quadrupole formula (at least in the sense of order estimate), since the typical time scale of the bosenova is rather long,  $\Delta t \sim 500M$ , and the nonrelativistic approximation can be applied.

The quadrupole moment  $Q_{ij}$  of the axion cloud is estimated to be  $Q_{ij} \sim r_p^2 E$ , where  $r_p \sim 10M$  is the position of the peak with respect to the  $r$  coordinate. In the bosenova collapse, a burst of positive energy flux toward the horizon is generated, and about 5% of the total energy falls into the BH in the typical time  $\Delta t \sim 500M$ .

It causes decrease in  $Q_{ij}$  through loss of the energy. Here, we ignored the shedding of the axion cloud to a far region because this process is slower than the burst to the horizon. Let us consider the situation where the decay constant  $f_a$  is the GUT scale, and hence, the bosenova collapse occurs at the energy  $E \approx 1.6 \times 10^{-3}M$ . Assuming the time dependence of energy as  $E = E_0 + (\Delta E/2)[\cos(\pi t/\Delta t) - 1]$  ( $0 \leq t \leq \Delta t$ , where the bosenova happens at  $t = 0$  and ends at  $t = \Delta t$ ) with  $\Delta E \approx 0.05E$ , we have

$$\ddot{Q}_{ij} \sim r_p^2 \ddot{E} \sim r_p^2 \Delta E \left(\frac{\pi}{\Delta t}\right)^3 \sim 10^{-9}. \quad (6.1)$$

From this, the energy loss rate is estimated to be  $dE/dt \sim (\ddot{Q}_{ij})^2 \sim 10^{-18}$ , and the total radiated energy is  $E_{\text{rad}} \sim 10^{-15}M \sim 10^{-12}E$ . Therefore, the energy converted to gravitational waves is expected to be very small in the bosenova. In a similar manner, we can estimate the amplitude of gravitational waves emitted in this process as

$$h \sim \frac{\ddot{Q}_{ij}}{r_{\text{obs}}} \sim 10^{-7} \frac{M}{r_{\text{obs}}}, \quad (6.2)$$

where  $r_{\text{obs}}$  denotes the distance from the BH to an observer.

For the supermassive BH at the center of our galaxy, Sagittarius A\*, the mass and the distance from the Sun have been estimated to be  $M \approx 4.5 \times 10^6 M_\odot$ <sup>(27), (28)</sup> and  $r_{\text{obs}} \approx 8 \text{ kpc}$ <sup>(28), (29)</sup>. For these values, we have  $M/r_{\text{obs}} \sim 10^{-11}$ , and therefore,  $h \sim 10^{-18}$ . The frequency of gravitational waves emitted in this process is  $\sim 1/\Delta t \sim 10^{-4} \text{ Hz}$ . The strain amplitude  $h_{\text{rss}} := [\int |h|^2 dt]^{1/2}$  of the gravitational wave burst in this process is  $h_{\text{rss}} \sim 10^{-16}(\text{Hz})^{-1/2}$ , and for the frequency  $10^{-4} \text{ Hz}$ , this value is (by order one) above the threshold of the sensitivity of the future-planned space-based gravitational wave detector, the LISA.<sup>(30)</sup> For the BH candidate Cygnus X-1, the mass and the distance have been estimated to be  $M \approx 8.7 \pm 0.8 M_\odot$ <sup>(31)</sup> and  $r_{\text{obs}} \approx 1.86_{-0.11}^{+0.12} \text{ kpc}$ <sup>(32)</sup>. For these values, we have  $M/r_{\text{obs}} \sim 10^{-16}$ , and therefore,  $h \sim 10^{-23}$ . The frequency of gravitational waves emitted in this process is  $\sim 100 \text{ Hz}$ . The strain amplitude is  $h_{\text{rss}} \sim 10^{-24}(\text{Hz})^{-1/2}$ , and for the frequency  $100 \text{ Hz}$ , this value is below the threshold of the sensitivity of the planned ground-based gravitational wave detectors, the Advanced LIGO, the Advanced Virgo, and the LCGT.<sup>(30)</sup>

Note that the estimate here has been done for the parameters  $\alpha_g = M\mu = 0.4$ ,  $a/M = 0.99$ , and  $f_a = 10^{16} \text{ GeV}$ . For other parameters, e.g. if the value of  $f_a$  is smaller, the detection of gravitational waves from the bosenova collapse is more difficult. However, if the value of  $f_a$  is around the GUT scale or somewhat larger, we have the possibility of detection of gravitational wave bursts from the bosenova. Although we have discussed only bursts here, it is also interesting to study gravitational waves that originate from the oscillation of the axion cloud during the bosenova whose period is  $\sim 10M$ . Since this oscillation continues at least for  $\sim 1000M$ , the detection may be more plausible. Also, it is interesting to take account of the possibility of existence of unknown BHs in the neighborhood of the Sun, because all existing candidates for stellar mass BHs are X-ray binaries while many isolated BHs that cannot be seen by electromagnetic waves are expected to exist.



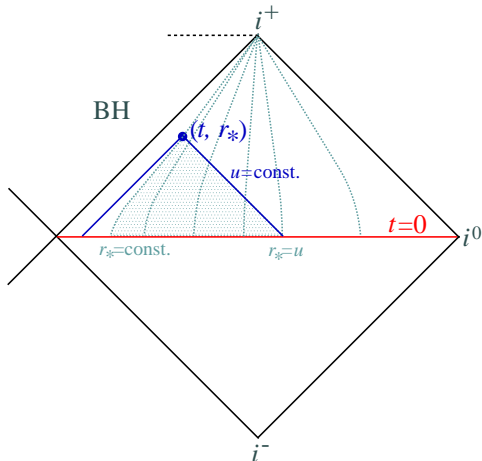


Fig. 18. The domain of integration shown in the Penrose diagram of a Kerr spacetime.

The detailed studies on the gravitational wave emission in the BH-axion system during the bosenova are necessary in order to improve the above rough estimate and to obtain indication of the existence of axionlike particles or constraints on them. Another interesting observational possibility is that if the BH is immersed in the magnetic field and the axion field  $\Phi$  has coupling to the electromagnetic field through the Chern-Simons interaction  $\mathcal{L}_{a\gamma\gamma} = g_{a\gamma\gamma} \Phi \mathbf{E} \cdot \mathbf{B}$ , the axion cloud may radiate electromagnetic waves. Studying the feature of the electromagnetic radiation in this process and exploring the possibility of observing this phenomena are also interesting issues to be investigated.

### Acknowledgements

H.Y. thanks Hajime Sotani, Hisa-aki Shinkai and Kunihiro Ioka for helpful comments. This work was supported by the Grant-in-Aid for Scientific Research (A) (22244030).

### Appendix A

#### — Green's function analysis —

In this appendix, we study which modes are generated by the nonlinear effect when the amplitude of  $\varphi$  is relatively small using a perturbative approach with the Green's function method. In particular, we pay attention to whether waves of  $(\ell, m) = (1, -1)$  mode found in our simulations can be generated. We decompose the field as

$$\varphi(x) = \varphi_0(x) + \Delta\varphi, \quad (\text{A}\cdot 1)$$

where  $\varphi_0$  is the bound state of the  $(\ell, m) = (1, 1)$  mode of the Klein-Gordon equation:

$$\varphi_0 = 2\text{Re} \left[ e^{(\gamma - i\omega_0)t} P(r) S_1^1(\cos\theta) e^{i\phi} \right], \quad (\text{A}\cdot 2)$$

and  $\Delta\varphi$  denotes the deviation generated by the nonlinear effect. In the following, we consider the situation where  $\varphi_0$  is relatively small, and take account of the order up to  $O(\varphi_0^3)$  and ignore terms of  $O(\varphi_0^4)$ . Then, the sine-Gordon equation is approximated as

$$(\square - \mu^2)\Delta\varphi = J, \quad (\text{A}\cdot 3)$$

with

$$J := -\frac{\mu^2}{6}\varphi_0^3 \quad (\text{A}\cdot 4)$$

Equation (A·3) is a linear equation with a source term  $J$ . In order to solve this type of equation, the Green's function method is useful. The Green's function is defined by

$$(\square' - \mu^2)G(x, x') = \delta^4(x, x'), \quad (\text{A}\cdot 5)$$

where  $x$  and  $x'$  denote some points in the spacetime, and hereafter, prime ( $\prime$ ) indicates the coordinates  $x'$ . Assuming the initial condition at  $t = 0$  to be  $\Delta\varphi = \partial_t(\Delta\varphi) = 0$ , the solution of  $\Delta\varphi$  is written in terms of the Green's function as

$$\Delta\varphi = \int_{D'} d^4x' \sqrt{-g(x')} G(x, x') J(x'). \quad (\text{A}\cdot 6)$$

Here, for  $x = (t, r_*, \theta, \phi)$  and  $x' = (t', r'_*, \theta', \phi')$ , the domain  $D'$  is taken as the triangular region  $u' \leq u$ ,  $v' \leq v$ , and  $t' \geq 0$ , where  $u$  and  $v$  are null coordinates,  $u = t + r_*$  and  $v = t - r_*$  (see Fig. 18).

The Green's function can be constructed in terms of the eigenfunctions of the operator  $\square - \mu^2$ . The specific form is

$$G(x, x') = \frac{1}{(2\pi)^2} \sum_{\ell, m} \int_{-\infty}^{\infty} d\omega G_{\ell m}^\omega(r, r') e^{-i\omega(t-t') + im(\phi-\phi')} S_\ell^m(\cos\theta) \bar{S}_\ell^m(\cos\theta'), \quad (\text{A}\cdot 7)$$

where bar denotes the complex conjugate and

$$G_{\ell m}^\omega(r, r') = \frac{1}{W_{\ell m\omega}} [\theta(r - r') R_{\ell m\omega}^+(r) R_{\ell m\omega}^-(r') + \theta(r' - r) R_{\ell m\omega}^-(r) R_{\ell m\omega}^+(r')]. \quad (\text{A}\cdot 8)$$

Here,  $R_+$  and  $R_-$  are radial functions satisfying the boundary conditions

$$R_{\ell m\omega}^+ \simeq \begin{cases} e^{ikr}/r, & r \rightarrow \infty; \\ A_{\ell m}^{[+]\omega} e^{i\tilde{\omega}r_*} + B_{\ell m}^{[+]\omega} e^{-i\tilde{\omega}r_*}, & r \simeq r_+, \end{cases} \quad (\text{A}\cdot 9)$$

$$R_{\ell m\omega}^- \simeq \begin{cases} A_{\ell m}^{[-]\omega} e^{-ikr}/r + B_{\ell m}^{[-]\omega} e^{ikr}/r, & r \rightarrow \infty; \\ e^{-i\tilde{\omega}r_*}, & r \simeq r_+, \end{cases} \quad (\text{A}\cdot 10)$$

where  $k = \sqrt{\omega^2 - \mu^2}$  and we impose  $\text{Im}[k] \geq 0$ . The function  $R^+$  is the solution satisfying the outgoing/decaying boundary condition at infinity, and the function  $R^-$  is the solution satisfying the ingoing boundary condition at the horizon. Choosing  $R^+$  and  $R^-$  in this way, the solution  $\Delta\varphi$  satisfies both of the ingoing boundary

condition at the horizon and the outgoing/decaying condition at infinity.  $W_{\ell m \omega}$  is the Wronskian determined by

$$W_{\ell m \omega}(R^-, R^+) := \Delta(-R^+ \partial_r R^- + R^- \partial_r R^+). \quad (\text{A}\cdot 11)$$

The value of  $W_{\ell m \omega}$  is constant for arbitrary  $r$ , and it is calculated as

$$W_{\ell m \omega}(R^-, R^+) = 2i\tilde{\omega}(r_+^2 + a^2)A_{\ell m}^{[+]\omega} = 2ikA_{\ell m}^{[-]\omega}. \quad (\text{A}\cdot 12)$$

Since we do not know the analytic expressions of  $R^-$  and  $R^+$  in the whole region  $r_+ \leq r < \infty$ , we cannot derive the exact solution. However, we can extract various properties of the solution of  $\Delta\varphi$ .

Substituting the Green's function (A.7) into Eq. (A.6), we have the following formula:

$$\Delta\varphi = \sum_{\ell, m} \int_{-\infty}^{\infty} d\omega e^{-i\omega t + im\phi} S_{\ell}^m(\cos\theta) [R_{\ell m \omega}^+(r)X_{\ell m \omega}^+(t, r) + R_{\ell m \omega}^-(r)X_{\ell m \omega}^-(t, r)], \quad (\text{A}\cdot 13)$$

where  $X_{\ell m \omega}^+$  and  $X_{\ell m \omega}^-$  are defined by

$$X_{\ell m \omega}^+(t, r) = \frac{1}{W_{\ell m \omega}} \int_{-v}^{r^*} dr' \frac{\Delta'}{r'^2 + a^2} \int_0^{v+r'} dt' e^{i\omega t'} R_{\ell m \omega}^-(r') J_{\ell m \omega}(t', r'), \quad (\text{A}\cdot 14)$$

$$X_{\ell m \omega}^-(t, r) = \frac{1}{W_{\ell m \omega}} \int_{r_*}^u dr' \frac{\Delta'}{r'^2 + a^2} \int_0^{u-r'} dt' e^{i\omega t'} R_{\ell m \omega}^+(r') J_{\ell m \omega}(t', r'), \quad (\text{A}\cdot 15)$$

with

$$J_{\ell m \omega} = -\frac{1}{(2\pi)^2} \int_0^{2\pi} d\phi \int_{-1}^1 d\nu (r^2 + a^2\nu^2) e^{-im\phi} S_{\ell}^m(\nu) U'_{\text{NL}}(\varphi_0), \quad (\text{A}\cdot 16)$$

where  $\nu := \cos\theta$ . Here, we introduce further approximation: we replace the spheroidal harmonics  $S_{\ell}^m e^{im\phi}$  by the spherical harmonics  $P_{\ell}^m e^{im\phi}$ . Although this approximation holds only when  $|a^2 k^2|$  is small, this formula is assumed for all values of  $\omega$ . In this approximation,  $J_{\ell m \omega}$  becomes independent of  $\omega$ , and therefore, we simply denote it by  $J_{\ell m}$ . Then, the integration can be performed as

$$J_{\ell m} = K_{\ell}^m(r) e^{(3\gamma - im\omega_0 t)} P(r)^{\frac{3+m}{2}} \bar{P}(r)^{\frac{3-m}{2}}. \quad (\text{A}\cdot 17)$$

where

$$K_3^{\pm 3} = \frac{\mu^2}{12\sqrt{210}\pi} (9r^2 + a^2), \quad (\text{A}\cdot 18a)$$

$$K_3^{\pm 1} = \frac{\mu^2}{20\sqrt{14}\pi} (3r^2 - a^2), \quad (\text{A}\cdot 18b)$$

$$K_1^{\pm 1} = \frac{3\mu^2}{140\pi} (7r^2 + a^2), \quad (\text{A}\cdot 18c)$$

and  $K_{\ell}^m = 0$  for the other values of  $\ell$  and  $m$ .

Now, let us consider the point  $(t, r)$  in the neighborhood of the horizon, i.e.,  $r \simeq r_+$ . For this point, it can be directly checked that  $X_{\ell m \omega}^+(t, r) \simeq 0$ , and therefore,  $\Delta\varphi$  satisfies the ingoing boundary condition at the horizon. On the other hand,  $X_{\ell m \omega}^-(t, r)$  becomes nonzero and can be written

$$X_{\ell m \omega}^-(t, r) = \frac{1}{W_{\ell m \omega}} \int_{r_*}^u dr' \frac{\Delta'}{r'^2 + a^2} \frac{e^{[3\gamma + i(\omega - m\omega_0)](u - r'_*)} - 1}{3\gamma + i(\omega - m\omega_0)} \times R_{\ell m \omega}^+(r') K_{\ell}^m(r') P(r')^{\frac{3+m}{2}} \bar{P}(r')^{\frac{3-m}{2}}. \quad (\text{A}\cdot 19)$$

Substituting this formula into Eq. (A·13), we get

$$\Delta\varphi = \sum_{\ell, m} e^{im\phi} S_{\ell}^m(\cos\theta) \frac{e^{im\Omega_H r_*}}{2i(r_+^2 + a^2)} \times \left\{ e^{(3\gamma - im\omega_0)u} D_{\ell m}(u, r_*) - \int_{-\infty}^{\infty} d\omega \frac{e^{-i\omega u}}{\tilde{\omega} A_{\ell m}^{[+]\omega} [3\gamma + i(\omega - m\omega_0)]} E_{\ell m}^{(\omega)}(u, r_*) \right\}, \quad (\text{A}\cdot 20)$$

with

$$D_{\ell m}(u, r_*) = \int_{-\infty}^{\infty} d\omega \frac{1}{\tilde{\omega} A_{\ell m}^{[+]\omega} [3\gamma + i(\omega - m\omega_0)]} \times \int_{r_*}^u dr' \frac{\Delta'}{r'^2 + a^2} e^{-[3\gamma + i(\omega - m\omega_0)]r'_*} R_{\ell m \omega}^+(r') K_{\ell}^m(r') P(r')^{\frac{3+m}{2}} \bar{P}(r')^{\frac{3-m}{2}} \quad (\text{A}\cdot 21)$$

and

$$E_{\ell m}^{(\omega)}(u, r_*) = \int_{r_*}^u dr' \frac{\Delta'}{r'^2 + a^2} R_{\ell m \omega}^+(r') K_{\ell}^m(r') P(r')^{\frac{3+m}{2}} \bar{P}(r')^{\frac{3-m}{2}}. \quad (\text{A}\cdot 22)$$

Here,  $D_{\ell m}(u, r_*)$  and  $E_{\ell m}(u, r_*)$  are slowly varying functions with respect to  $u$  and  $r_*$  for  $r_* \ll -M$  and  $u \gg M$ .

Let us consider the first term of Eq. (A·20). The dependence of the first term on  $t$  and  $\phi$  is  $\sim e^{3\gamma t + im(\phi - \omega_0 t)}$ , and this is a mode propagating to  $+\phi$  direction. The integration of the second term is performed using the techniques of the complex analysis. Defining the contour  $C$  in a complex  $\omega$  plane that goes along the real line from  $-\infty$  to  $\infty$  and then clockwise along a semicircle centered at zero in the lower-half plane, the integral is rewritten as the sum of contribution from the poles and the integration along the branch cut. Since the branch cut integral typically gives a subdominant contribution, we focus attention to the poles. The singular points of the integrand appear at  $\omega = m\Omega_H$ ,  $\pm\mu$ ,  $m\omega_0 + 3\gamma$ , and  $\omega_{\text{BS}}^{(\ell mn)}$  satisfying  $A_{\ell m}^{[+]\omega_{\text{BS}}^{(\ell mn)}} = 0$  ( $n = 1, 2, 3, \dots$ ). Among them,  $\omega = m\Omega_H$  and  $\pm\mu$  become endpoints of the branch cut, and therefore, they are not poles. By applying the residue theorem to the poles  $\omega = m\omega_0 + 3i\gamma$  and  $\omega_{\text{BS}}^{(\ell mn)}$ , the terms proportional to  $e^{3\gamma t + im(\phi - \omega_0 t)}$  and  $e^{i(m\phi - \omega_{\text{BS}}^{(\ell mn)} t)}$  appear, respectively. Among these two,  $e^{3\gamma t + im(\phi - \omega_0 t)}$  represents waves propagating in the  $+\phi$  direction.

In order to understand the behavior of  $e^{i(m\phi - \omega_{\text{BS}}^{(\ell mn)} t)}$ , we have to evaluate  $\omega_{\text{BS}}^{(\ell mn)}$ .

From Eq. (A·9), the condition  $A_{\ell m}^{[+]\omega_{\text{BS}}^{(\ell mn)}} = 0$  gives the mode satisfying the ingoing boundary condition at the horizon and the decaying/outgoing boundary condition at infinity simultaneously. This is the bound state discussed in Sec. 2. The typical mode of the bound state satisfies  $\omega_{\text{BS}}^{(\ell mn)2} \simeq \mu^2 \simeq \omega_0^2$ , since the gravitational binding energy is not so large. Then, typical value of  $\omega_{\text{BS}}$  is estimated as

$$\omega_{\text{BS}}^{(\ell mn)} \simeq \pm \omega_0. \quad (\text{A}\cdot 23)$$

Remember that the poles for the bound states typically appear in both right and left half complex planes. If we adopt  $m = 1$ , the behavior of  $e^{i(m\phi - \omega_{\text{BS}}^{(\ell mn)} t)}$  becomes  $e^{i(\phi \mp \omega_0 t)}$ , and the waves of negative frequency  $\omega_{\text{BS}}^{(\ell mn)} \simeq -\omega_0$  propagate to the  $-\phi$  direction (i.e., they are waves of the  $m = -1$  mode).

### References

- 1) A. Arvanitaki, S. Dimopoulos, S. Dubovsky, N. Kaloper and J. March-Russell, Phys. Rev. D **81** (2010), 123530, arXiv:0905.4720.
- 2) A. Arvanitaki and S. Dubovsky, Phys. Rev. D **83** (2011), 044026, arXiv:1004.3558.
- 3) H. Kodama and H. Yoshino, arXiv:1108.1365.
- 4) R. D. Peccei and H. R. Quinn, Phys. Rev. Lett. **38** (1977), 1440.
- 5) R. D. Peccei and H. R. Quinn, Phys. Rev. D **16** (1977), 1791.
- 6) G. Mocanu and D. Grumiller, arXiv:1203.4681.
- 7) S. L. Cornish, N. R. Claussen, J. L. Roberts, E. A. Cornell and C. E. Wieman, Phys. Rev. Lett. **85** (2000), 1795, cond-mat/0004290.
- 8) E. A. Donley, N. R. Claussen, S. L. Cornish, J. L. Roberts, E. A. Cornell, and C. E. Wieman, Nature **412** (2001), 295, cond-mat/0105019.
- 9) H. Saito and M. Ueda, Phys. Rev. Lett. **86** (2001), 1406, cond-mat/0002393.
- 10) H. Saito and M. Ueda, Phys. Rev. A **63** (2001), 043601, cond-mat/0006410.
- 11) H. Saito and M. Ueda, Phys. Rev. A **65** (2002), 033624, cond-mat/0107248.
- 12) E. W. Leaver, Proc. Roy. Soc. Lond. A **402** (1985), 285.
- 13) S. A. Hughes, Phys. Rev. D **61** (2000), 084004 [Errata; D **63** (2001), 049902, D **65** (2002), 069902, D **67** (2003), 089901], gr-qc/9910091.
- 14) R. A. Breuer, M. P. Ryan Jr, and S. Waller, Proc. R. Soc. London **A358** (1977), 71.
- 15) E. Seidel, Class. Quant. Grav. **6** (1989), 1057.
- 16) E. Berti, V. Cardoso and M. Casals, Phys. Rev. D **73** (2006), 024013 [Errata; D **73** (2006), 109902], gr-qc/0511111.
- 17) Y. B. Zel'dovich, Pisma Zh. Eksp. Teor. fiz. **14** (1971), 270, JETP Lett. **14** (1971), 180.
- 18) Y. B. Zel'dovich, Zh. Eksp. Teor. fiz. **62** (1972), 2076, Sov. Phys. JETP **35** (1972), 1085.
- 19) W. H. Press and S. A. Teukolsky, Nature **238** (1972), 211.
- 20) T. Damour, N. Deruelle and R. Ruffini, Lett. Nuovo Cim. **15** (1976), 257.
- 21) S. L. Detweiler, Phys. Rev. D **22** (1980), 2323.
- 22) T. J. M. Zouros and D. M. Eardley, Ann. of Phys. **118** (1979), 139.
- 23) H. Furuhashi and Y. Nambu, Prog. Theor. Phys. **112** (2004), 983, gr-qc/0402037.
- 24) M. J. Strafuss and G. Khanna, Phys. Rev. D **71** (2005), 024034, gr-qc/0412023.
- 25) V. Cardoso and S. Yoshida, J. High Energy Phys. **0507** (2005), 009, hep-th/0502206.
- 26) S. R. Dolan, Phys. Rev. D **76** (2007), 084001, arXiv:0705.2880.
- 27) S. Gillessen, F. Eisenhauer, S. Trippe, T. Alexander, R. Genzel, F. Martins and T. Ott, Astrophys. J. **692** (2009), 1075, arXiv:0810.4674.
- 28) A. M. Ghez *et al.*, Astrophys. J. **689** (2008), 1044, arXiv:0808.2870.
- 29) F. Eisenhauer *et al.*, Astrophys. J. **597** (2003), L121, astro-ph/0306220.
- 30) M. Pitkin, S. Reid, S. Rowan and J. Hough, Living Rev. Relativity **14** (2011), 5, arXiv:1102.3355.
- 31) N. Shaposhnikov and L. Titarchuk, Astrophys. J. **663** (2007), 445, astro-ph/0703441.

- 32) M. J. Reid, J. E. McClintock, R. Narayan, L. Gou, R. A. Remillard and J. A. Orosz, *Astrophys. J.* **742** (2011), 83, arXiv:1106.3688.